Simulation and Testing of Wavefront Reconstruction Algorithms for the Deformable Mirror (DeMi) Cubesat

by

Gregory W. Allan

B.S., Northeastern University (2016)

Submitted to the Department of Aeronautics and Astronautics
in partial fulfillment of the requirements for the degree of

Master of Science in Aeronautics and Astronautics

at the

MASSACHUSETTS INSTITUTE OF TECHNOLOGY

September 2018

Author .....
Department of Aeronautics and Astronautics
August 23, 2018

Certified by .....
Kerri Cahoy
Associate Professor
Thesis Supervisor

Accepted by .....
Hamsa Balakrishnan
Chair, Graduate Program Committee

Simulation and Testing of Wavefront Reconstruction Algorithms for the Deformable Mirror (DeMi) Cubesat

by

Gregory W. Allan

Submitted to the Department of Aeronautics and Astronautics
on August 23, 2018, in partial fulfillment of the
requirements for the degree of
Master of Science in Aeronautics and Astronautics

Abstract

The search for exoplanets has discovered thousands of worlds orbiting stars other than our own. To learn more about these worlds, it is necessary to directly image them and study their atmospheric spectra. Especially of interest are Earth-like planets, but they are typically outshined by their host stars by a factor of 10^{10}, meaning high-contrast imaging is required to see them. Coronagraphs are typically used to block the starlight to achieve high contrast, but atmospheric, thermal, and mechanical aberrations can cause spurious speckles of starlight to contaminate the image. Use of space telescopes removes atmospheric aberrations, but other sources still remain. In order to achieve the optical performance necessary for high-contrast imaging, adaptive optics (AO) techniques in space are needed. High actuator count deformable mirrors (DMs) used in an AO system enable the required contrasts across sufficient fields of view, but typically have high size, weight, and power requirements, and can be complex to implement. New technologies such as Micro-electromechanical Systems (MEMS) DMs can potentially alleviate these problems. MEMS DMs also have applications in high-energy lasers, optical communications, and imaging systems. However, MEMS DMs have not been sufficiently tested in an orbital environment. While environmental tests can be performed on the ground, on-orbit operation in vacuum with exposure to radiation for extended periods cannot be sufficiently simulated. If MEMS DMs are to gain acceptance for use in future space missions, interactions with other system components must be studied, and support systems suitable for operating the DM in the space environment with constrained size, power, and computation resources must be developed. This thesis discusses the Deformable Mirror Demonstration Mission (DeMi), which aims to address these needs. Specifically, we develop and demonstrate wavefront sensing approaches suitable for demonstrating and characterizing a MEMS DM on a small satellite platform.

Thesis Supervisor: Kerri Cahoy
Title: Associate Professor

Acknowledgments

I am deeply grateful to my advisor, Kerri Cahoy, who has provided invaluable guidance and technical direction throughout my graduate studies. Without her advice and encouragement this thesis would not have been possible.

I would like to acknowledge Ewan Douglas, the driving force behind the DeMi mission, and a wonderful teacher and collaborator. Ewan's enthusiasm for adaptive optics and astronomy inspired me to choose this thesis topic. I would also like to thank Bobby Holden, Christian Haughwout, John Merk, and the rest of the DeMi team for their hard work making this project a reality.

Lastly, I'm grateful to Katie Morzinski of the University of Arizona and the rest of the staff of the Summer School for Adaptive Optics, which provided an ideal learning environment to improve my understanding of adaptive optics in the final stages of writing this thesis.

This work at MIT has been sponsored by DARPA under a contract with Aurora Flight Sciences, a Boeing Company.

Contents

List of Figures

List of Tables

Chapter 1

Introduction and Motivation

1.1 Introduction

The purpose of this thesis is to study methods for validating the performance of the microelectromechanical systems (MEMS) Deformable Mirror (DM) on the Deformable Mirror Demonstration Mission (DeMi) CubeSat. To motivate this work, the importance of MEMS DMs and the DeMi CubeSat to the field of astronomy is presented, specifically the direct imaging of exoplanets (planets outside our solar system). The particular role of MEMS DMs in their use for exoplanet direct imaging provides guidance for assessment of the wavefront sensing and control techniques developed in this thesis. The focus of this work is on wavefront reconstruction and phase retrieval techniques rather than on closed-loop control.

1.1.1 Adaptive Optics

The central problem of Adaptive Optics (AO) is to correct the shape of a non-uniform incoming optical phase front [1]. AO is typically used for ground-based astronomy, where light from a distant object reaches the top of the Earth's atmosphere effectively as a plane wave. The flat wavefront then interacts with the turbulent atmosphere on its way to a ground-based telescope. The wavefront is disturbed by this process, as different parts of the wavefront are delayed by air with different temperatures and

thus different density and index of refraction. An aberrated wavefront results in an imperfect Point Spread Function (PSF) and a blurry image. In order to take an image of the target without distortion, this wavefront must be corrected before it is focused on to the imager. A common method for wavefront correction involves the use of a separate optical wavefront sensor to measure the aberrated phase, and an active element such as a DM which uses the measured phase information to actuate a complementary shape and remove the aberration. An example of this arrangement is shown in Figure 1-1. For a detailed treatment of AO concepts, refer to [2].

The drawback of using a separate wavefront sensor is that it is located separately from the main optical path of the science instrument so the light must be split using additional optical elements. Misalignments or imperfections of elements in the optical paths induce additional phase aberrations in each wavefront, referred to as non-common-path errors [2]. One way to avoid these errors is by eliminating the separate wavefront sensor and using the main optical sensor to measure the shape of the wavefront [3].

1.1.2 AO Applications

In addition to the typical astronomical imaging application, AO is applicable to a wide variety of technical problems. AO was first developed and demonstrated for the application of using telescopes to image satellites in Earth orbit [2], and it remains a key tool for space situational awareness. Other uses of AO for atmospheric compensation are in optical communications between terminals on the ground, in the air, and in space [5], and in airborne directed-energy weapons [6]. On a smaller scale, AO is used in optometry to detect aberrations in the lens of the human eye, and to improve the imaging properties of optical microscopes in biological samples [7]. In this work, we focus on the use of MEMS DMs with AO techniques for exoplanet direct imaging.

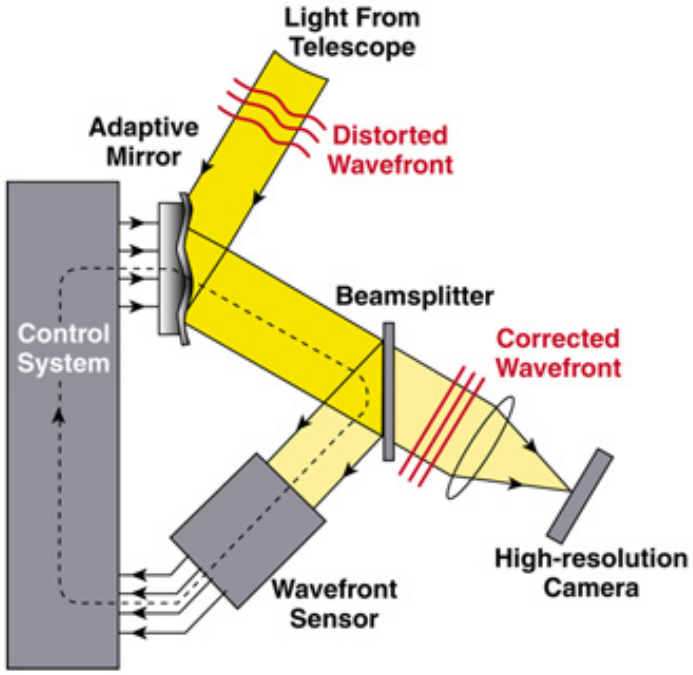

Figure 1-1: A typical adaptive optics system [4]. Phase retrieval methods could reduce the need for a separate wavefront sensor in some cases.

1.1.3 High-Contrast Imaging

Planets outside of our solar system (exoplanets) are being detected by operational observatories in space and on the ground. To date over 3800 confirmed exoplanets have been discovered [8], of many different sizes and distances to their parent stars. Particularly of interest is the search for potentially habitable planets. In most cases, this refers to planets of a similar mass to Earth in the habitable zones of their parent stars.

The typical methods of exoplanet detection are indirect, measuring a host star's position (radial velocity) [9] and brightness (transit detection) [10]. These methods are useful for discovery and measurement of the planets' masses and orbital periods, but they provide limited information about the composition of planetary atmospheres and the structure of debris disks and planet-forming regions. Taking a direct image of the planetary system enables spectroscopy and the detection of other structures [11]. Spectroscopy of light reflected from exoplanets is critical to understanding the

chemical makeup of their atmospheres, which could potentially contain biosignatures indicating the presence of life.

The main challenge in obtaining a direct image is that the parent star is brighter than the planet by a factor of 10^{10} in the case of an earth-like planet in the habitable zone of a sun-like star. All light from the parent star must be occluded to a 10^{10} level if the planetary signal is to be distinguished from the star.

One way to block the parent star's light is with a coronagraph, using an amplitude or phase mask in the optical instrument. Amplitude masks must be effectively apodized in order to reduce diffracted light. Phase masks, such as the vector vortex coronagraph [12] are increasingly adopted due to their smaller Inner Working Angle (IWA). Since the contrast between star and planet is so high, tolerances on potion of the coronagraph mask, and on the amount of light diffracted by telescope structures or scattered by imperfections in optics, are extremely tight.

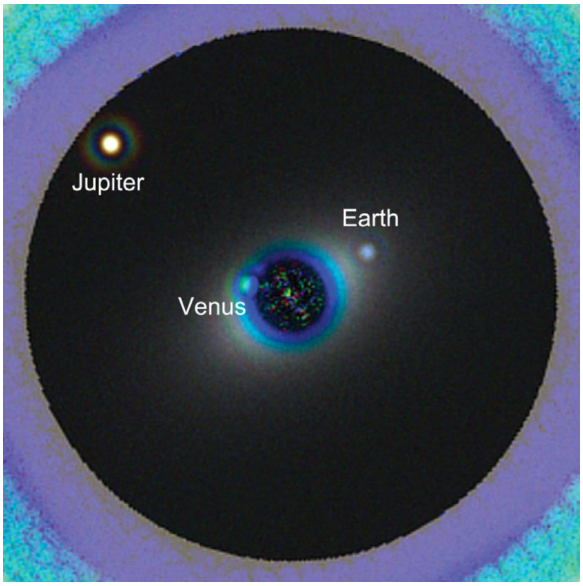

Figure 1-2: Simulated image of our solar system viewed through a Lyot coronagraph at a distance of 13.5 parsecs. The IWA is shown just smaller than the orbit of Venus, while the OWA is shown just larger than the orbit of Jupiter. [13]

AO is required for exoplanet direct imaging because aberrated wavefronts cause light to diffract through coronagraphs even though they are designed for optimal performance. Imaging at contrast levels of 10^{10} requires wavefronts that are controlled

to the order of $\lambda/10{,}000$ [11]. Manufacturing tolerances, telescope motion, thermal variations, and atmospheric turbulence make this an impossibility without active control. Even with AO, atmospheric aberrations cannot be corrected up to contrasts sufficient for imaging earthlike exoplanets, so space telescopes are needed, as discussed in Section 1.1.4.

A coronagraph creates a region at the image plane with a very low incidence of starlight. As seen in Figure 1-2 the inner and outer working angle of the system impact its ability to image planets close to and far from their host star, respectively. IWA is primarily determined by the parameters of the coronagraph itself, while OWA is determined by the parameters of the DM. Specifically, a larger number of DM actuators across the pupil increases the OWA because higher spatial frequency DM perturbations can scatter light at a larger angle. This relationship is shown by:

$$\theta_{outer} = \frac{N\lambda}{2D} \tag{1.1}$$

Where N is the number of DM actuators across the pupil and D is the diameter of the aperture [11].

1.1.4 AO in Space

The ability of AO systems to correct atmospheric aberrations puts a fundamental limit on the contrast achievable by ground-based telescopes. For a 100 m telescope, the limit is on the order of 10^8, which is insufficient to image most Earth-like exoplanets [14, 15]. This makes space telescopes extremely valuable in the search for life in solar systems similar to our own. Even for space-based platforms, adaptive optics systems are necessary in order to counter the effects of diffraction and optical imperfections. Regardless of atmospheric aberrations, manufacturing technology necessary to fabricate relatively large optics and complicated optical assemblies to $\lambda/10{,}000$ accuracies for high-contrast imaging do not yet exist.

AO is still important for a wide range of space telescope systems even though they do not have to combat atmospheric distortion, because of manufacturing limita-

tions and because of the challenging launch and space environments. Accelerations, shocks, and vibrations experienced during the launch of a spacecraft can cause displacement or deformation of optical elements. Misalignments cause static wavefront aberrations in the optical path that cannot be corrected without active elements. Temperatures on board can swing by more than 50 degrees Celsius in a matter of minutes as the spacecraft enters and exits eclipse. Thermal variation and gradients over spacecraft structures can cause differential expansion, displacing and distorting of optical elements. Spacecraft also commonly carry reaction wheels or thrusters for attitude control, and inherent imperfections in these components can cause vibrations that induce quickly time-varying aberrations. AO systems can measure and correct these problems in real time, improving the quality of optical measurements on space platforms.

Adaptive optics can also potentially enable transformative concepts for deployable, self-assembling and other reconfigurable telescope systems [16, 17]. For instance, AO can allow a system to adapt to imperfections in the deployment mechanism of a telescope aperture that has been folded and stowed in order to conform to launch vehicle constraints.

A distinction can be made between "adaptive" and "active" optical systems. Systems to correct align telescope structures based on external metrology, or to correct slowly-varying errors with limited degrees of freedom, are typically referred to as active. Devices used to respond to quickly time-varying aberrations and correct higher-order wavefront modes are considered adaptive. In this thesis, we focus on the use of DMs, traditionally an adaptive optics tool. We apply them to correct aberrations at high and low rates, at high and low order spatial modes. For convenience, we use the term "adaptive" to apply to all of these regimes.

1.1.5 MEMS Deformable Mirrors

Deformable mirrors used on AO systems can be based on one of several different technologies, but Micro-electromechanical systems (MEMS) DMs are a compelling option for high-contrast imaging and for space applications. They are manufactured

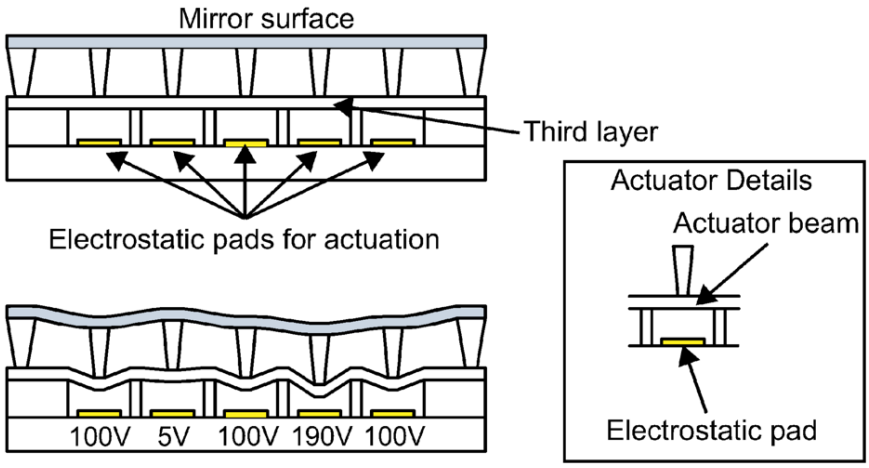

Figure 1-3: Schematic view of a MEMS DM [19].

from a silicon substrate [18], and consist of a continuous membrane with a reflective coating over an array of electrostatic actuators. Each actuator comprises a parallel plate capacitor, and when charged with a voltage typically between 0V and 250V, the plates attract, deforming the mirror surface. An illustration of the MEMS DM structure is shown in Figure 1-3.

MEMS DMs are appropriate for use in space because their lower size, weight, and power (SWaP) when compared to piezo-electric, electrostrictive, or voice coil designs allows easier accommodation in spacecraft, and their low actuator mass makes them resilient to launch-induced vibrations. Their high actuator density enables higher actuator counts for a given pupil size. Reduction of pupil size allows reduction of the size and weight of optics across the system, which is beneficial for constrained space applications. Actuator counts of at least 128 across the pupil have been proposed for future exoplanet direct imaging missions [20]. MEMS DMs are typically square, with 128 x 128 actuators giving 16,384 in this example. Though they are particularly well-suited, these devices have not yet been extensively tested in the space environment.

Other MEMS optical devices have flown in space previously, including a single micro-mirror on the MEMS Telescope for Extreme Lightning (MTEL) [21, 22], and a microshutter array [23]. A high-actuator count MEMS DM has been operated briefly during a sub-orbital sounding rocket flight, and survived reentry and subsequent impact with the ground at high speed [24]. However, additional validation is needed

to show that MEMS DMs are suitable for long-term in-space use on an operational telescope. The devices will need to withstand radiation effects, spacecraft charging, long-term temperature cycling, and extended operation in vacuum. Long-term environmental effects are difficult to replicate in a lab environment, so an actual low Earth orbit (LEO) mission is needed to validate the technology.

1.2 The DeMi Mission

The DeMi mission is a technology demonstration intended to enable future space missions using MEMS DMs [25, 26, 27]. The preparation for this mission also provides risk reduction for the challenging development of flight software, electronics hardware, and mechanical packaging necessary to operate a DM in space. The top-level requirements for the mission (MIS) as defined in the DeMi System Requirements Review documentation [28] are shown in Table 1.1.

DeMi will provide valuable data on the survivability of MEMS DMs for extended operation in an orbital environment, and raise the technology readiness level (TRL) of MEMS DM hardware from TRL 6 [24] to at least TRL 7 (requirement L1-MIS-01). The mission will also demonstrate closed-loop wavefront control in space, correcting slowly-varying, high-order aberrations as well as quickly-varying tip-tilt errors (requirement L1-MIS-02). Closed-loop, in-space wavefront control with a MEMS DM is currently at a TRL of 5 [29, 30, 31], and DeMi will also raise this TRL to 7.

Requirement L1-MIS-03 captures the need to test the DM in a realistic AO application. The spacecraft will therefore measure the PSFs of stars. Stars provide a light source on which to perform wavefront control. The imaging system needed for PSF measurement provides a model of a typical in-space instrument whose operation would benefit from AO technology. Executing closed-loop wavefront control on a broadband stellar source is necessary to fully demonstrate the feasibility of AO with MEMS DMs in space. The requirement also highlights DeMi's usefulness as a tool for science when on-orbit, as stellar photometry can be applied to transiting exoplanet observations [26].

Requirement L1-MIS-04 states that the system must enable reprogramming of the payload software while on orbit. It refers directly to the need to compare the performance of different wavefront sensing methods. Such experimentation is itself valuable for the advancement of AO technology. The final mission requirement (L1-MIS-05) is that the spacecraft must be built in accordance with the standard CubeSat specification. This requirement ensures compatibility with parts and service providers. It will reduce the cost and time required to develop the mission, and make it easier to secure a launch. The CubeSat Standard is further discussed in Section 1.2.1.

Designator	Description	Requirement
L1-MIS-01	DM Operation in Space	DeMi shall demonstrate the operation of a MEMS deformable mirror in space.
L1-MIS-02	Wavefront Correction in Space	DeMi shall measure and correct wavefront phase aberrations in space.
L1-MIS-03	Observe Stars	DeMi shall measure stellar point spread functions and photometric intensities.
L1-MIS-04	Wavefront Retrieval Algorithms	DeMi shall include the capability to reprogram payload software on-orbit.
L1-MIS-05	CubeSat	DeMi shall be built in accordance with the standard CubeSat architecture.

Table 1.1: DeMi Mission Requirements

1.2.1 The CubeSat Standard

The CubeSat standard is an open specification for a family of small spacecraft formats [32]. The initial specification was for a an approximately 10 cm x 10 cm x 10 cm cube, now known as a single CubeSat unit (1U). CubeSats as large as 12U have been developed.

The standard has been instrumental in reducing the cost and time to put a spacecraft into orbit. Its existence has led to standardized spacecraft deployers which can be manifested on launch vehicles. Spacecrafts can now more easily find a ride to orbit at a reduced price, while the launch provider has an avenue to monetize excess capacity on their vehicles which might otherwise simply be filled with ballast.

1.3 Thesis Contributions

This thesis focuses on the design and development of the wavefront sensing approach for the DeMi CubeSat. Chapter 2 provides an overview of the DeMi satellite and its requirements. In this context, we consider and assess wavefront sensing techniques used to meet mission requirements and objectives. In Chapter 3, methods for wavefront sensing with a Shack-Hartmann Wavefront Sensor (SHWFS) are discussed, and the selected approach is explained in detail, along with supporting simulation and experimental results. Chapter 4 discusses a different approach called image plane wavefront sensing, and presents simulations and experimental results for using image plane wavefront sensing for DeMi. In Chapter 5, methods for calibration and validation of the optical payload and MEMS DM are presented. Chapter 6 summarizes the results of this thesis work and suggests future work towards the completion of the DeMi project.

Chapter 2

Approach

2.1 Overview of the DeMi CubeSat

In order to satisfy the mission requirements (Table 1.1) and the lower-level system and subsystem requirements [28], the DeMi mission uses the Blue Canyon Technologies XB6 platform. The XB6 is a 6U (30 cm x 20 cm x 10 cm) spacecraft bus comprising solar panels, batteries, command and data handling electronics, communication systems, and Attitude Determination and Control System (ADCS). For DeMi, the bus contains a Cadet-U UHF radio capable of receiving commands from the ground and downlinking data to the 18 m dish at NASA Wallops Flight Facility at a nominal rate of 1 Mbps. It also includes an Astrodev Lithium 2 UHF radio for backup communications at up to 9.6 kbps. The backup UHF ground station is located on the MIT campus in Cambridge, MA.

The XB6 bus includes the XACT ADCS, which is made up of a star tracker, an inertial measurement unit, magnetic torque rods, and reaction wheels. The system is capable of accurately pointing the bus with stability better than 10 arcseconds (1σ) in all axes [33]. The spacecraft systems occupy about 1.5U of the spacecraft volume, leaving the remaining 4.5U for payload systems. The payload is designed to satisfy the science and payload requirements shown in Tables 2.1 and 2.2, and is discussed in Section 2.1.2

2.1.1 Science and Payload Requirements

The DeMi System Requirements Review document [28] specifies a hierarchy of Mission, System, and Subsystem requirements. For this thesis, we focus on key level 2 Science (SCI) and level 3 Payload (PAY) requirements that pertain to the wavefront sensing system. The science requirements are shown in Table 2.1. The first two of these directly address the wavefront sensing capability. L2-SCI-01 requires that wavefront displacements from DM actuators be measured to a precision of 12 nm. Displacing a DM surface results in a change in path-length for rays that hit the surface. Since the rays travel to the surface and then back in the reflected direction, this path length difference is twice the DM surface displacement. Therefore, L2-SCI-01 requires measurement of changes to the DM surface with a precision of 6 nm. L2-SCI-02 requires that low-order aberrations be measured to an accuracy of $\lambda/10$ and a precision of $\lambda/50$. At a nominal wavelength of 635 nm, these distances correspond to 63.5 nm and 12.7 nm respectively.

Requirements L2-SCI-03 and L2-SCI-04 state that the system must correct static and dynamic wavefront errors to less than 100 nm RMS. Static wavefront errors might be caused by residual misalignments in the optical assembly, or could be displacements induced by acceleration or shock during launch or deployment. Dynamic errors might be caused by thermal variation over short timescales, or by actuator disturbances such as reaction wheel jitter.

The relevant PAY requirements are shown in Table 2.2 and are derived from the four SCI requirements shown in Table 2.1. L3-PAY-02 specifies that wavefront corrections must be made to 100 nm RMS error for displacement and spatial frequencies within the capability of the DM.

L3-PAY-01 requires that measurements of the wavefront for DM characterization be performed at the stated 6 nm precision. L3-PAY-03 specifies that the low-order Zernike modes to be measured to $\lambda/10$ accuracy and $\lambda/50$ precision should be: tilt, focus, astigmatism, coma, and spherical aberration. These disturbances have a much lower spatial frequency than the compact influence functions of DM actuator pokes.

L3-PAY-09 places requirements on the image sensor in a SHWFS. Specifically, lenslet spots must be centroided to 0.01 pixels. The SHWFS configuration is discussed in Chapter 3.

L3-PAY-05 states that wavefront corrections must be applied at 12 Hz or faster. This requirement is derived from a CubeSat fine pointing stage analysis in [34]. The 12 Hz rate constrains the choice of wavefront control algorithms used. Wavefront control is discussed in Section 2.2.3.

Designator	Description	Requirement
L2-SCI-01	Measure Displacement	The payload shall measure individual deformable mirror actuator wavefront displacement contributions to a precision of 12 nm.
L2-SCI-02	Measure Low Order Modes	The payload shall measure low order aberrations to $\lambda/10$ accuracy and $\lambda/50$ precision.
L2-SCI-04	Static WFE correction	The payload shall correct static wavefront phase errors up to the spatial frequency and stroke capabilities of th DM, to less than 100 nm RMS.
L2-SCI-05	Dynamic WFE Correction	The payload shall correct dynamic wavefront phase errors up to the spatial frequency and stroke capabilities of th DM, to less than 100 nm RMS.

Table 2.1: Selected DeMi Science Requirements

2.1.2 The DeMi Payload

The DeMi payload is an electro-optomechanical system hosted on the CubeSat bus. It contains the DM, optics to provide a stable wavefront, sensors to measure DM performance, and electronics to operate the DM, read out sensor data, and perform wavefront control.

In order to meet DeMi mission requirements a dual-sensor architecture was chosen early in the design process. An image-plane sensor is included to meet the requirement of measuring stellar PSFs (L1-MIS-03) and a standalone pupil-plane wavefront sensor (SHWFS) is included as it is better suited for measuring and correcting wavefront errors (L1-MIS-02). This configuration is similar that of an astronomical AO

Designator	Description	Requirement
L3-PAY-01	Measurement Accuracy	The payload wavefront sensor shall measure DM surface errors up to the spatial frequency and stroke capabilities of th DM, to precision better than 6 nm RMS.
L3-PAY-02	Correction Accuracy	The payload shall correct static wavefront phase errors up to the spatial frequency and stroke capabilities of th DM, to less than 100 nm RMS.
L3-PAY-03	Measure Zernikes	The WFS shall measure the internal RMS surface error due to tilt, focus, astigmatism, coma, and spherical aberration to 32 nm accuracy with 6 nm precision.
L3-PAY-05	Speed	The payload shall perform wavefront error measurement and apply corrections to the DM surface in a closed loop at at 12 Hz or faster.
L3-PAY-09	Centroiding	The payload wavefront sensor detector shall permit PSF centroiding to 0.01 pixels using the internal laser source.

Table 2.2: Selected DeMi Payload Requirements

system. Both sensors are based on the same commercial, off-the-shelf (COTS) industrial CMOS camera, the Pixelink PL-D775MU-BL, with an ON Semiconductor MT9P031 5-megapixel sensor. The SHWFS uses a Thorlabs MLA150-5C microlens array to create the necessary spot field. Discussion of the choice of wavefront sensing techniques follows in Section 2.2.

The DeMi payload provides two separate sources of light for measuring the DM surface: an external aperture to admit light from a star, and an internal laser diode with stable output power. A ray-trace of the optical system is shown in Figure 2-2. The external aperture is defined by a baffle with a rectangular stop and illuminates an aluminum off-axis parabola (OAP) mirror. The stellar image is focused onto a field mirror, and then collimated into a beam by another OAP before being directed at the DM. The beam is then split such that half the light is focused onto a CMOS imager. The remaining light from the pupil plane is relayed to a SHWFS. A single-mode fiber (SMF) is embedded in the field mirror, and its other end is pigtailed onto a 2.5 mW, 635 nm laser diode (Thorlabs LPS-635-FC) such that it can provide an additional source of light for wavefront sensing in the event that sufficient pointing accuracy for

stellar imaging cannot be maintained.

A rectangular aperture is used to perfectly illuminate the shape of DM. The collimated light from the aperture hits the DM at a roughly 45 degree angle, so the square DM appears as a rectangle in collimated space. Over-filling the DM would result in an improperly corrected PSF when wavefront control is used, while under-filling it would prevent the measurement of the performance of actuators near the edge of the DM and reduce the sensitivity of the imaging system.

The whole payload assembly is mounted on an aluminum optical bench which is affixed to the CubeSat bus with three titanium standoffs. The standoffs form an approximate kinematic constraint while providing thermal and vibrational isolation from the bus.

2.1.3 Electrical Design

The DeMi payload electronics stack consists of a power distribution board, two DM driver boards, and two Raspberry Pi Compute Module 3 processor boards. A block diagram of the DeMi payload electronics is shown in Figure 2-1. These boards are configured as a stack in a sub-1U form factor with stacking board-to-board electrical connectors precluding the necessity for major inter-component harnessing. Ribbon cables are used to connect the DM driver boards to the DM. Power is provided by the XB6 bus in three channels that can be independently switched by bus commands; one at 5V and two at 3.3V. High-voltage (250V) and -5V power for the DM controller is generated on the power distribution board. A constant-current power supply will be mounted beside the stack and used to drive the internal laser diode.

2.2 Wavefront Sensing Approach

The primary wavefront sensor in the DeMi payload is a SHWFS. In addition to this dedicated wavefront sensor, DeMi includes an image-plane sensor to capture stellar PSFs. Since the imager is read out by an independent payload computer, it can continue to operate in the event of a failure of the wavefront sensing computer.

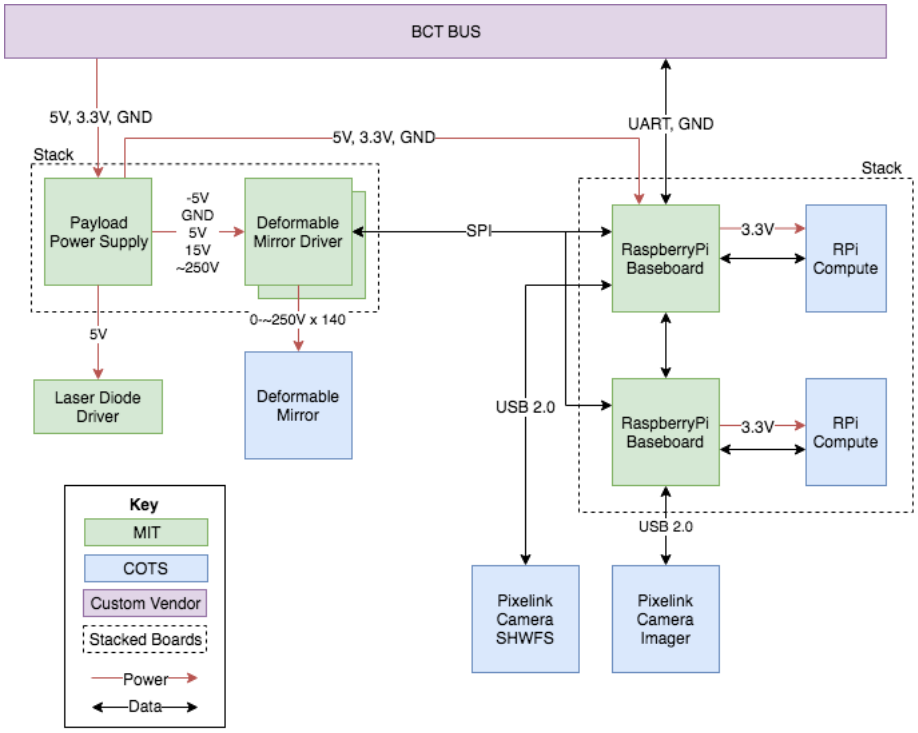

Figure 2-1: Block diagram of the DeMi electronics system. Most boards are part of one electronics stack, as indicated by the dotted line. The stack is held together by standoffs between boards, with header connectors to provide electrical connections along the stack. The key shows which components are designed by the DeMi payload team at MIT and which come from external vendors.

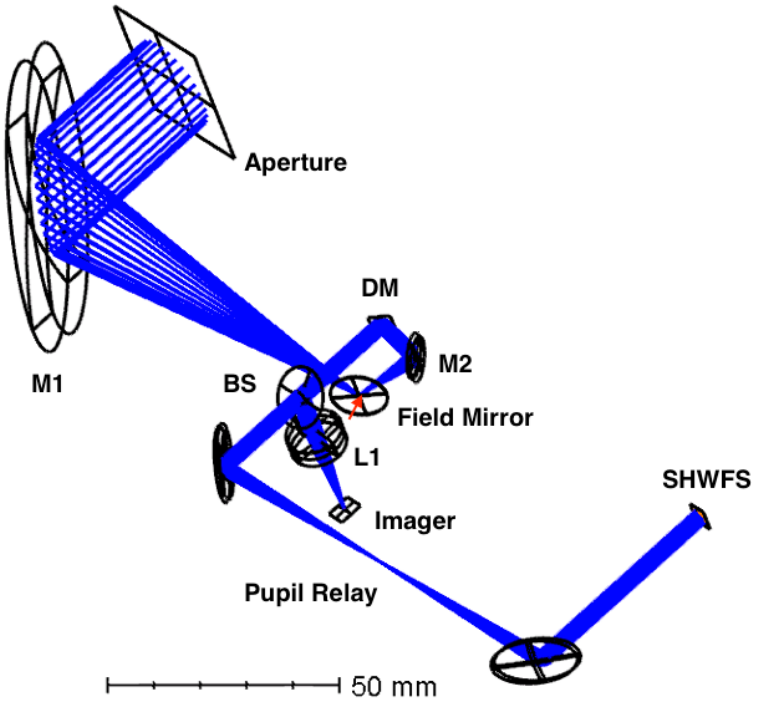

Figure 2-2: Ray trace of the DeMi payload optical layout performed in Zemax for an on-axis stellar source, incident from the aperture in at the top via a baffle (not shown). The red arrow indicates the site for injection of a laser source via a single-mode optical fiber in the center of the field mirror,

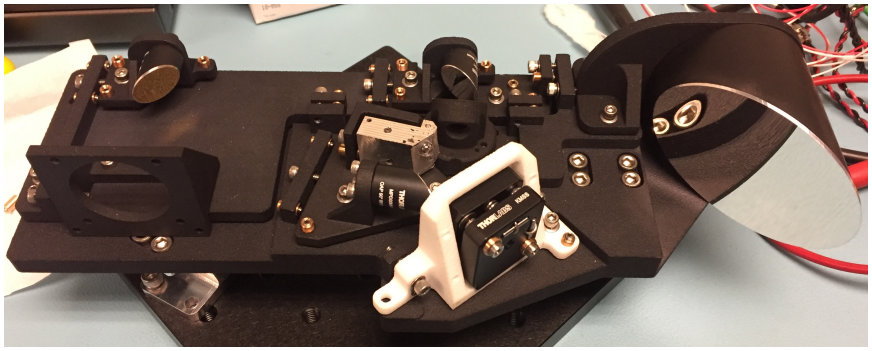

(a)

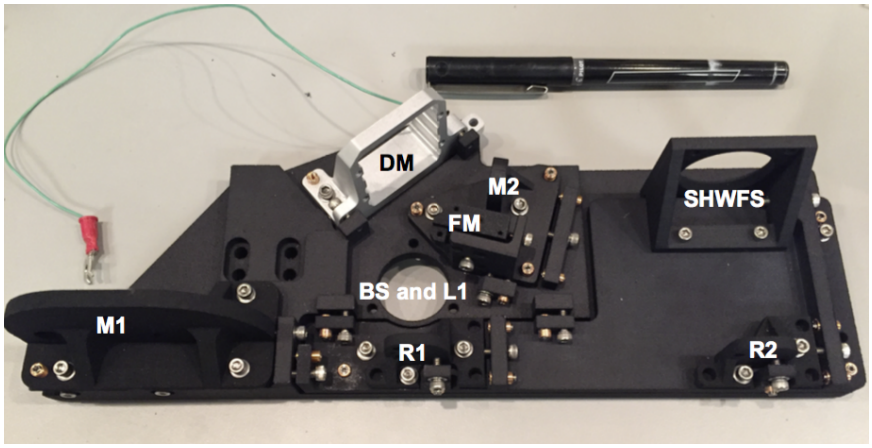

(b)

Figure 2-3: (a) 3D-printed prototype of the DeMi Payload optical assembly. (b) Labeled, top-down view of the prototype.

Enabling some wavefront sensing functionality on the imaging camera has the benefit of introducing failure-tolerance into the payload design.

2.2.1 Discrete Wavefront Sensors

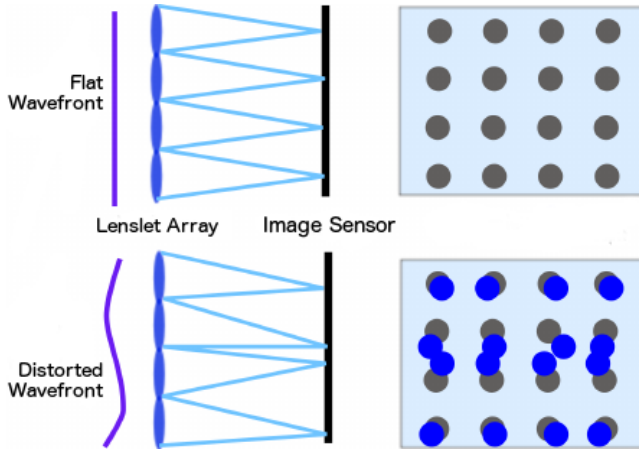

Figure 2-4: Theory of operation for SHWFS lenslet array. Figure adapted from [35].

There are several types of wavefront sensing technologies commonly used in AO systems, including wavefront curvature sensing [36], pyramid wavefront sensing [37], and Shack-Hartmann wavefront sensing (SHWFS). A pyramid wavefront sensor can operate with a dim light source [38], but the variant with no moving parts has small dynamic range [39]. The modulated pyramid WFS has higher dynamic range, but its use would require an additional electro-optical actuator. Curvature wavefront sensing similarly requires actuators, while the SHWFS has no moving parts and is easily implemented with COTS components.

The SHWFS is made up of an image sensor behind an array of small lenslets as shown in Figure 2-4. It works on the principle that a slope in a wavefront incident on a lens will induce a displacement in the focal spot of that lens. By using an array of lenslets, we sample the local gradients of the incoming wavefront in each lenslet aperture. A flat wavefront creates focused PSFs in line with the optical axis of each lenslet. A distorted wavefront will cause the positions of these focal spots to shift in two dimensions according to the local gradients. This principle is illustrated in Figure 2-4. A SHWFS has the drawback that splitting the aperture into many

sub-apertures reduces the amount of light in each focal spot, thus decreasing the signal-to-noise ratio (SNR) of the measurement. Reconstruction of wavefront shape from slope measurements can be performed using a zonal or modal approach; in this work a zonal fit is used and is discussed in detail in Chapter 3.

2.2.2 Image Plane Wavefront Sensing

One of the drawbacks of a discrete sensor such as a SHWFS is the non-common-path error between it and the science camera. If the camera itself can be used for wavefront sensing, then these errors can be eliminated. On DeMi, enabling WFS with the science camera has the added benefit of fault tolerance in the case of a failure of the SHWFS or its processor.

The simplest form of sensing that can be done with the camera is detection of tip-tilt errors. We can easily compute the average slope of the incoming wavefront based on displacement of the PSF centroid using the same concept as the SHWFS.

Sensing of higher-order disturbances can be performed, but is not straightforward. The basic challenge is to calculate the amplitude and phase of the field in the pupil plane based on only intensity measurements in the image plane. This problem is discussed in detail in Chapter 4 This class of problems is known as phase retrieval. Many techniques to solve them are iterative and rely on assumptions about the geometry of the optical system, including aperture shape and illumination of the pupil [40]. In practice these quantities are difficult to measure or estimate with enough precision to get adequate results. The Gerchberg-Saxton [41] algorithm is perhaps the most well-known and straightforward of these. It was implemented and simulated for this thesis, but laboratory experiments did not yield a solution. Discussion of the technique and results is included in Appendix A.

Other techniques decrease their reliance on models by incorporating more than one image-plane measurement [42]. The additional measurements are taken in different conditions, such as slightly defocusing the PSF. Different measurements provide phase diversity which can break the ambiguities inherent in a single PSF intensity image. However, these techniques require actuators to change the system configuration, and

any motions typically must be measured precisely in order to correctly calculate the pupil phase.

The differential optical transfer function (dOTF) method is a new approach that can use DM actuations to provde the necessary phase diversity, by adding a perturbation to the wavefront near the edge of the pupil [3]. dOTF also doesn't require exact knowledge of that perturbation in order to calculate the result. Its use has been suggested for space telescope wavefront sensing [43], but to the knowledge of the author, it has not yet been employed. Use of this relatively new algorithm is therefore in line with requirement L1-MIS-04. The dOTF method is discussed in depth in Chapter 4.

2.2.3 Wavefront control

The DeMi mission includes the demonstration of closed-loop wavefront control on orbit. This thesis does not treat closed-loop control in depth, but the topics of sensing and control are inherently linked. The DeMi payload will have to correct both static and dynamic aberrations typical of space telescopes as described in Section 1.1.4. The dynamic aberrations will be caused by spacecraft reaction wheel jitter, and will mostly be characterized by tip-tilt errors in the wavefront. They occur at temporal frequencies in the 10s of Hz. Thermal variations occur on a slower timescale of seconds to minutes, and can cause optical misalignments, inducing aberrations such as defocus, astigmatism, and coma. Launch-induced misalignments will also cause aberrations of the same order, but should be static once DeMi reaches orbit.

The differing temporal and spatial frequencies of the aberrations make it convenient to correct them in two distinct modes. The high-order static and thermal variations are corrected at a rate of 1-3Hz using the output of the SHWFS as an error signal. The SHWFS spot displacements can either be used directly to calculate DM actuator voltages, or the reconstructed wavefront can be used. The control bandwidth required and processing capability of the DeMi payload drive the way that the SHWFS data is incorporated into the closed-loop controller, as wavefront reconstruction is more computationally intensive.

Tip-Tilt Correction

The high-speed tip-tilt variations will be corrected at a rate of 36 Hz, faster than the 12 Hz required in L3-PAY-05. The error signal for this correction is a subset of the SHWFS lenslet spots. The control rate is limited to 36 Hz by the ability to read out a full SHWFS image and perform the required calculations to apply control voltages. Since only tip-tilt information is needed, it is sufficient to use only the displacements from a single row and column of lenslet spots, approximating an average spot displacement over the aperture. This saves computation time and allows correction at a faster rate than the high spatial order control loop. To add redundancy to the tip-tilt correction system, the correction can also be accomplished without the SHWFS, using displacement of the PSF in the science imager.

2.3 Concept of Operations

The concept of operations (ConOps) defines the planned tasks that will be performed over the course of the DeMi mission. The first steps are launch, deployment, and commissioning of the satellite systems. When the payload is powered on, the first step is to perform an on-orbit calibration of the wavefront sensor systems, as discussed in Section 5.1.4. After calibration, the payload performs its wavefront sensing observations.

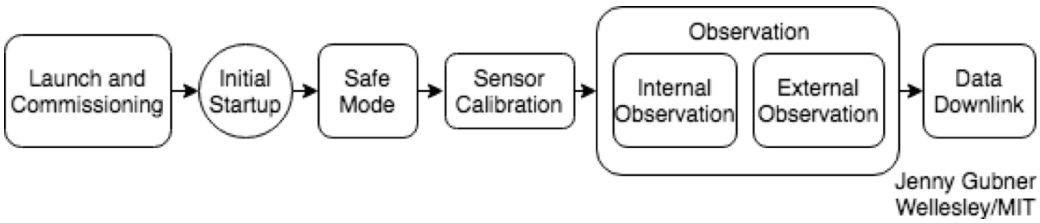

Figure 2-5: Diagram of the top-level concept of operations (CONOPS) for the DeMi mission.

The DeMi payload has two primary modes of observation. In the internal mode, the laser source is used to provide illumination of the DM. In the external mode, the spacecraft slews to point at a star.

Internal Mode

In internal mode, the spacecraft is left in its default attitude control state, optimizing for solar charging. Two types of tests can be performed on the payload in this mode. In closed-loop mode, wavefront control algorithms are used to flatten the wavefront of the test laser, and PSFs are measured at the image plane. Open-loop mode is more relevant to this thesis, and focuses on the characterization of DM actuator poke values.

In open-loop, the DeMi payload actuates each DM actuator at voltages of 0 V to 250 V, at intervals of 25 V. For each voltage, a SHWFS image is captured and wavefront reconstruction is performed. DM regions of 4×4 actuators are then actuated at the same voltages, and the resulting wavefronts are measured. Actuator displacements at each voltage are compared with baseline measurements taken during commissioning, and basic pass/fail information is stored for downlink. In the event of a measurement out of the expected range, the detailed wavefront data can be requested. It can also be downlinked in bulk during a contact with the high-rate radio. Single DM pokes provide verification that individual actuators are operating correctly, while 4×4 regions test that the DM is reaching its maximum stroke.

It will be more difficult to measure wavefronts for all voltages and actuators using the image-plane dOTF method since the results are higher resolution and so require more storage space. Additional analysis is needed to assess feasibility of capturing all dOTF measurements and to refine the ConOps accordingly.

External Mode

In the external mode, the spacecraft attitude control system is directed to point the payload aperture at a chosen stellar target. To take advantage of limited time on the target, only the closed-loop control of the AO system will be tested. In case of a failure in the laser source, this mode can also be used for DM actuator poke measurements as described above.

Chapter 3

Shack-Hartmann Wavefront Sensing

3.1 Wavefront Sensing Method

The primary method of wavefront sensing for DM characterization and wavefront control is with a SHWFS. As described in Chapter 2, a SHWFS translates local wavefront slopes into focal spot displacements on an image sensor. For the DeMi CubeSat, the quantity of interest is the shape of the DM surface, which is directly measured by the shape of the wavefront reflected from it. Therefore, we must reconstruct the wavefront shape from the spot displacement data. The absolute phase displacements of the wavefront surface on a sampling grid must be reconstructed from the local slopes of that surface. This problem, and the "zonal" approach to its solution are described in detail by Southwell [44]. The zonal formulation directly relates the points on the reconstruction grid to the local slope measurements from the WFS, and computes a best fit.

Another approach is to reconstruct the wavefront in terms of a set of orthogonal basis modes (functions). The set of Zernike polynomials [45] is one such basis that is commonly used in optics to represent wavefront errors. In this modal approach, the gradients of each mode are calculated and the coefficients of this new basis of slope modes are fit to the measured SHWFS slopes. The coefficients can then be used to reconstruct the wavefront displacements. This method has the benefit that it outputs Zernike coefficients which are more easily interpreted by researchers. In a

typical optical system, use of the modal method would enable easy diagnostics of the sources of Zernike terms such as defocus, astigmatism, and coma.

In the case of DeMi, the wavefront errors will intentionally be caused by displacements of individual actuators or regions of the DM, and so the values of the Zernike terms are of less interest. In order to accurately reconstruct the DM shapes, high-order spatial Zernike modes would need to be used. Another major disadvantage of the modal approach with Zernikes is that the Zernike modes are circular. If the reconstruction region differs from a circular spot, as is the case for DeMi's rectangular DM area, the edges of the modes cease to contribute to the wavefront fit and even higher modes are needed to capture higher spatial frequencies.

For DeMi, a zonal reconstruction approach is chosen due to its ease of application and its adaptability to different sizes of rectangular aperture. It is discussed in depth in Section 3.1.2. Before the wavefront reconstruction is begun, there are several steps of image processing that must be completed.

3.1.1 Image Processing and Centroiding

The first challenge in handling data from a SHWFS is the processing of image data into individual lenslet spot displacements. Data processing involves separation of the image into sub-images corresponding to each lenslet, centroiding of the focal spot to determine an exact spot location, and comparison of the spots locations with a baseline.

Before proceeding, we note that the baseline lenslet spot locations cannot simply be defined by the geometry of the system. Expecting spots to line up axially with lenslets when a flat wavefront is incident will result in consistent biases in the wavefront measurement. Small deviations in position and angle of the lenslet array when installed on the sensor will result in slight spot offsets, so instead the actual positions of the spots with a flat wavefront incident must be observed in a calibration procedure. We also note that the boundaries used to partition the image are most easily defined as boxes with the baseline spots in their centers. Both baseline spot position measurement and bounding box definitions are thus best performed prior to

SHWFS operation in a separate calibration procedure. In order to make a consistent comparison, the same centroiding algorithm should be used to calculate both the reference spot locations and the spot locations for each wavefront measurement. The centroiding method used in this thesis is a simple center-of-mass approach [46].

Lenslet Spot Calibration

The result of the calibration procedure should be a set of initial spot coordinates

$$p_0^{i,j} = \left(x_0^{i,j}, y_0^{i,j}\right) \qquad \begin{matrix} i = [1, m] \\ j = [1, n] \end{matrix} \tag{3.1}$$

where m and n are the dimensions of the lenslet array. Each spot coordinate is to be used in calculating spot displacements and as the center of a bounding box for centroiding when the sensor is running. For the wavefront sensing calculations, the spot coordinates must be indexed properly to reflect their relative positions such that $p_0^{0,0}$ neighbors $p_0^{0,1}$ and $p_0^{1,0}$. This ensures that the wavefront displacements are related properly by the measured slopes, which will derive their indices from the p_0 indices.

The image processing for this calibration is performed in Python because of the availability of powerful open-source image processing tools. Specifically, the scikit-image package [47] is used to partition the image into distinct spots based on their intensity. A uniform grid of points is then generated, whose spacing, position, and angle are manually adjusted to best match the spot positions. A centroid for each distinct spot is computed and true centroids are matched to grid indices based on their proximity to the points of the manually-tuned uniform grid. The grid of indexed spot coordinates is exported as comma-separated value (CSV) file for use at runtime.

The manual adjustment step could potentially be eliminated by more automation if necessary. The calibration only needs to be done once for a given setup, so will be performed before launch and likely once again while the satellite is on orbit. This will involve sending a single full-frame SHWFS image to the ground and sending the calculated centroid coordinate grid up to the spacecraft, which is within the capabilities of DeMi's data storage and communication systems. The overall calibration

procedure is discussed in more detail in Chapter 5.

The lenslet array used for lab testing has several spots that are of low brightness, or have asymmetrical PSFs as shown in Figure 3-1. This is likely due to improper handling of the lab lenslet array resulting in damage or surface contamination. Cleaning has not been attempted to avoid potential further damage. Proper handling procedures will be followed with the flight units, but this problem shows the need for flexibility in the wavefront reconstruction method in case similar contamination occurs.

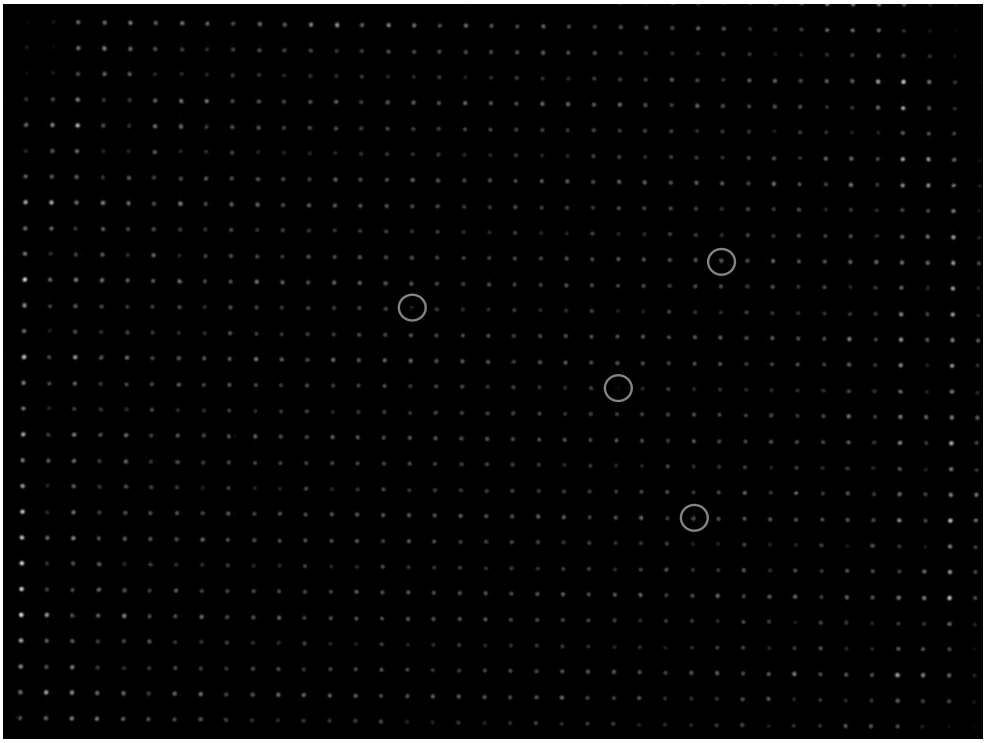

Figure 3-1: Image of lenslet spots from the DeMi Shack-Hartmann Wavefront Sensor. Note several faint or malformed focal spots. Brightness and contrast have been enhanced for visibility.

3.1.2 Zonal Reconstruction

There are three commonly-used geometries used for reconstructing wavefront phase for slope measurements, shown together in Figure 3-2. The Hudgin geometry uses x and y slope measurements that are displaced from each other and from the phase

reconstruction points, while the Fried geometry uses x and y slope measurements that are co-located, but offset from the phase points by one half step in each direction []. The Southwell geometry uses x and y slope measurements that are co-located with one another and with the phase reconstruction points. Both the Fried and Southwell geometries are suitable for representing a SHWFS, as a SHWFS measures both the x and y components of the wavefront gradient at each lenslet point. The following explanation applies to a square grid. Code for performing zonal reconstruction with a non-square rectangular grid included in Appendix D.

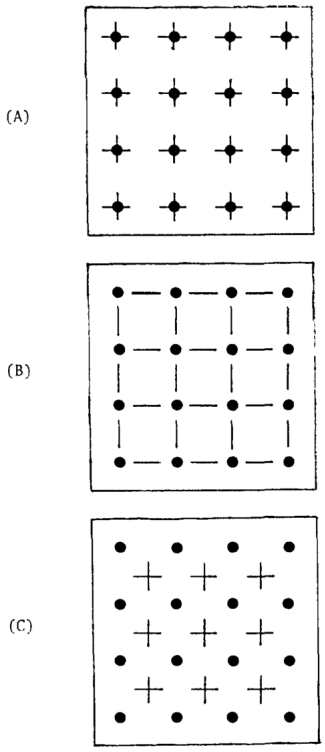

Figure 3-2: Three common model geometries used for reconstructing wavefront displacements from slope measurements: Southwell (A), Hudgin (B), and Fried (C). Dots represent displacement points for the reconstruction, while lines represent slope measurements in each direction [44].

In the Fried geometry, the wavefront phase ϕ_{ij} and the slopes in the x and y directions, s^x_{ij} and s^y_{ij} at indices ij can be related by:

$$s^x_{ij} = \frac{[\phi_{i+1,j} - \phi_{i+1,j+1}]/2 + [\phi_{ij} + \phi_{i,j+1}]/2}{h} \tag{3.2}$$

$$s_{ij}^{y} = \frac{[\phi_{i,j+1} - \phi_{i+1,j+1}]/2 + [\phi_{ij} + \phi_{i+1,j}]/2}{h} \tag{3.3}$$

In the Southwell Geometry, the wavefront phase ϕ_{ij} and the slopes in the x and y directions, s_{ij}^{x} and s_{ij}^{y} at a point (i, j) on the lenslet grid can be related to the slopes and phase at neighboring points by the following equations [44].

$$\frac{(s_{i+1,j}^{x} + s_{ij}^{x})}{2} = \frac{\phi_{i+1,j} - \phi_{ij}}{h} \qquad \begin{matrix} i = [1, N-1] \\ j = [1, N] \end{matrix} \tag{3.4}$$

$$\frac{(s_{i,j+1}^{y} + s_{ij}^{y})}{2} = \frac{\phi_{i,j+1} - \phi_{ij}}{h} \qquad \begin{matrix} i = [1, N] \\ j = [1, N-1] \end{matrix} \tag{3.5}$$

Where N^2 is the number of phase/slope points and h is the distance between those points (the lenslet pitch). Since the slope measurement points are co-located with the reconstruction points, we assume that the average slope between adjacent points is the average of the measured slopes at those points.

Though the Fried geometry is more commonly used for AO, it has the major drawback that it is insensitive to a set of modes known as "waffle" modes. These modes are characterized by neighboring phase points being alternately high and low. Since Eq. 3.2 and 3.3 relate the slopes to the averages of neighboring phase points, a reconstructor based on these relations will not be sensitive to equal and opposite displacements in those points. We proceed with the Southwell geometry primarily because it is sensitive to waffle modes.

There are methods which use the Fried and Southwell geometries, but with different mathematical formulations. Some methods use higher-order finite difference approximations to have enhanced spatial frequency response [48], and Fourier methods can be used for increased speed [49]. However, the finite difference method based on the Southwell geometry is easy to implement and adapt. Its suitability for the DeMi mission is evaluated in Section 3.3 and 3.4.

In order to solve Eqs. 3.4 and 3.5 for the phase displacements, we can write these equations in matrix form:

$$Ds = A\phi \tag{3.6}$$

where ϕ is a vector of phase displacements and s is a vector of phase displacement and measured slopes, with the x and y slope measurements concatenated. A is a finite difference matrix that approximates the first derivative between phase points, and D averages the slopes between adjacent lenslets. Algorithms for constructing these matrices for a square lenslet array can be found in [50]. As discussed in Chapter 2, the DeMi aperture will be constructed to illuminate the rectangular extent of the DM. Since the projection of the DM into collimated space is rectangular, a rectangular SHWFS configuration is be used. Discussion of a modification to the algorithm enabling construction of these matrices for a rectangular, rather than square, array can be found in appendix **??**.

Many techniques have been developed for least-squares solution of Equation 3.6. Iterative methods such as successive over-relaxation (SOR) [44], are commonly used to reduce memory and computation requirements. The computational resources on board DeMi are sufficient to use a straightforward matrix pseudoinverse approach based on singular value decomposition (SVD). This approach has the advantage that it gives the minimum-norm least-squares solution. The SOR method and other pseudoinverse formulations have infinitely many solutions, corresponding to the addition of a constant wavefront at every point. The SVD-based Moore-Penrose pseudoinverse gives the solution with both

$$||A\phi - Ds||_2 = \min \tag{3.7}$$

and

$$||\phi|| = \min \tag{3.8}$$

removing the ambiguity in overall phase [51].

3.2 Sensor Design

The DeMi SHWFS is made up of a PixeLink PL-D775MU-BL CMOS camera board, a Thorlabs MLA150-5C-M microlens array, and a custom aluminum case that serves

as a mount and a holder for the lenslet assembly. The DeMi SHWFS is shown in Figure 3-3. The parameters of the sensor assembly are collected in Table 3.1.

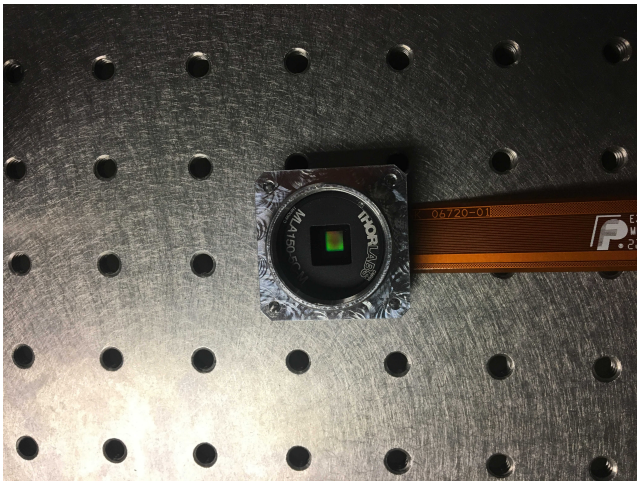

Figure 3-3: An image of the custom SHWFS designed for the DeMi mission,

Parameter	Value
Lenslet Pitch	150 um
Lenslet Diameter	146 um
Fill Factor	74.60%
Focal Length*	5.1 mm
Plate Scale	11.2 deg/mm
Pixel Size	2.2 um
Detector Size	2592 px x 1944 px
Lenslets on Sensor	36 x 28

Table 3.1: Parameters of the SHWFS on the DeMi payload. The lenslet array is a Thorlabs MLA150-5C, and the camera is a Pixelink PL-D775MU-BL. The camera datasheet is included in Appendix C.2. *Lenslet focal length as measured in Section 3.2.2.

3.2.1 Dynamic Range

The upper limit of SHWFS's ability to measure slopes is defined by the maximum displacement of each lenslet spot. When the spot travels outside of the radius of its lenslet, it can no longer be detected. The displacement δx of the spot due to a slope s is given by:

$$\delta x = sf \tag{3.9}$$

where f is the lenslet focal length. The maximum slope is therefore given by:

$$s_{max} = \frac{D}{2f} \tag{3.10}$$

We can compare the SHWFS's maximum slope to the requirement that it measure displacement and spatial frequencies up to the DM's capability. We consider that the maximum slope that can be induced on the surface of the DM occurs when a 4×4 region is actuated to its full stroke of 5.5 um. As a conservative approach, we treat the actuator region as if it is pinned at the edges, such that the slope on its sides is the stroke divided by twice the actuator pitch. For the Multi-5.5 flight DM, the slope is 0.012. The wavefront slope is twice this value. The DM's parameters can be found in Appendix C.1.1. Plugging the wavefront slope into Equation 3.9 gives a displacement of 62.3 um, which is within the 75 um radius of each lenslet.

3.2.2 Lenslet Focusing

The focal length of the lenslets is specified as 5.2 mm, but due to near-field effects, the effective focal length may be shorter. Therefore, it is necessary to manually focus the array at the proper distance from the sensor. This is accomplished with the use of steel shims. Lenslet spot images are captured with several shim thicknesses across the expected range of focal distance. The image is segmented into spots, and low-quality spots are identified as described in Section 3.1.1. Two-dimensional Gaussian distributions are fit to each spot, and the spotwidths are recorded. The average spot width for each configuration is plotted, as shown in Figure 3.2.2. The best focal distance is 0.005 in of shim material. Combined with the stack-up of PCB and mechanical parts, the resulting observed focal distance is approximately 5.10 mm.

3.3 Zonal Reconstruction Simulations

A test wavefront is generated using a random superposition of the first 21 Zernike polynomials. These correspond to the polynomials up to radial order 5. The Zernikes

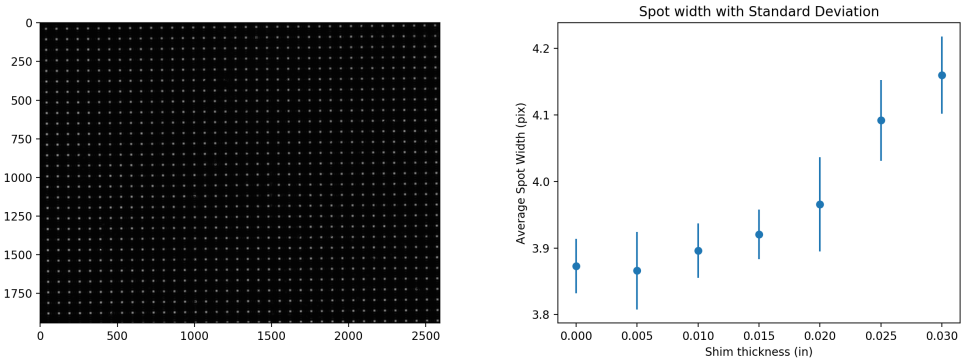

(a) (b)

Figure 3-4: Image of the SHWFS lenslet spots on the CMOS image sensor (a). Similar images are captured with different at different focal distances, and measured average spot widths are plotted in (b).

are calculated using the Physical Optics Propagation in PYthon (POPPY)[52] package. A simulated SHWFS with the same parameters as the DeMi SHWFS (Table 3.1) is used to generate spot displacement data for input to the wavefront reconstruction algorithm. The SHWFS simulator defines a grid of circular areas in a 2D plane, matching the dimensions of the DeMi SHWFS lenslet array. The simulated lenslets sample the input wavefront shape, and gradients of the wavefront are averaged over each lenslet area, resulting in x and y gradient components. These slopes are then input to the zonal reconstruction algorithm. The results of one such simulation are shown in Figure 3-5. The resulting RMS error is approximately 2.47 nm over a wavefront with a peak-to-valley of over 9 um. Such results are typical for the many observed simulation runs. These results satisfy the 32 nm RMS accuracy requirement in L3-PAY-03 over the 5.5 um maximum DM actuator stroke.

3.4 SHWFS Lab Testing

3.4.1 Lab Test Setup

A representative optical system containing a DM, image-plane sensor, and SHWFS is used to evaluate wavefront sensing methods. The objective of this test is to determine

the accuracy and precision of the sensing method across the range of DM actuations required on orbit, and compare the results to the Payload requirements. Single and 4×4 actuator pokes are used because they are the disturbances that L3-PAY-01 requires to be measured. Data relating actuator voltage to mirror displacement is provided by Boston Micromachines, and is a convenient ground-truth for determining accuracy. Since actuator pokes have higher spatial frequency, they are harder to

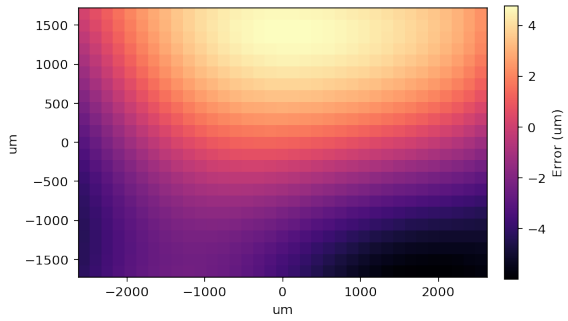

(a)

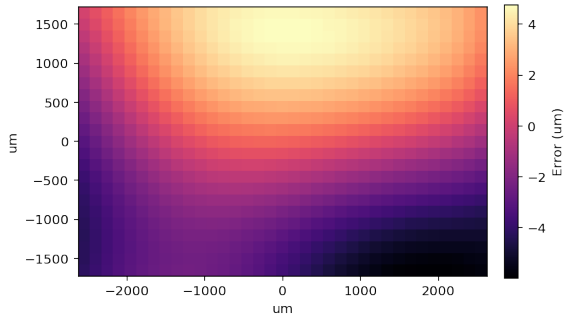

(b)

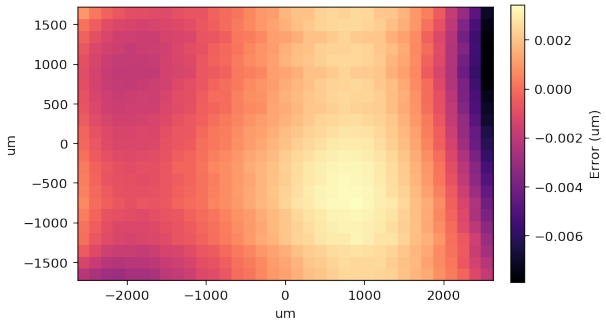

(c)

Figure 3-5: Results of the SHWFS simulation. The reconstructed phase is shown in (a), the ground-truth phase is in (b). The error between truth and reconstruction is shown in (c) with a different color scale.

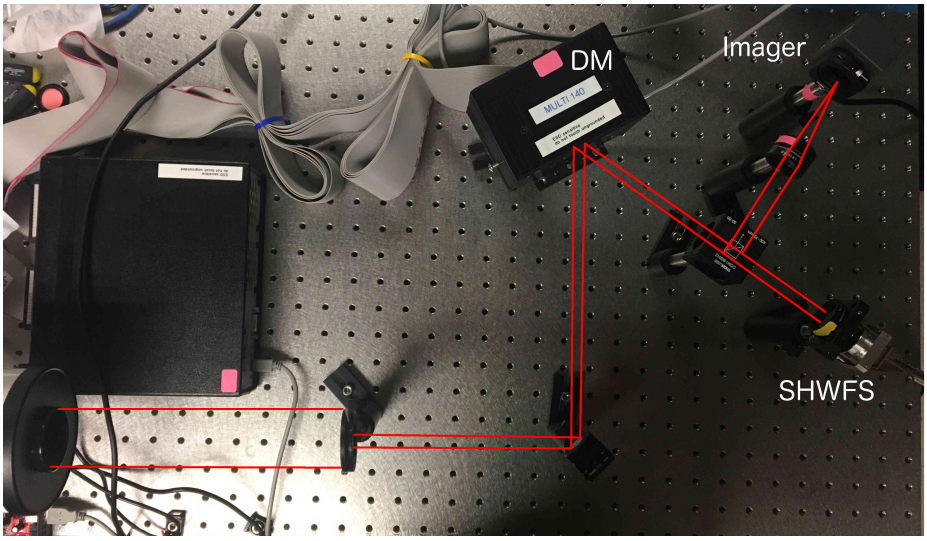

Figure 3-6: Laboratory setup used to test both SHWFS and image plane wavefront sensing methods.

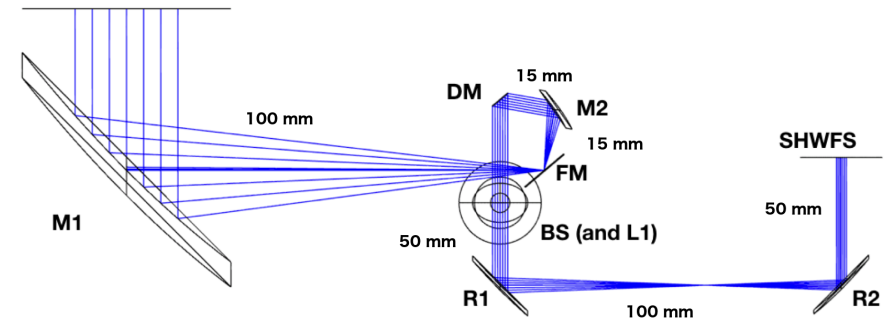

(a)

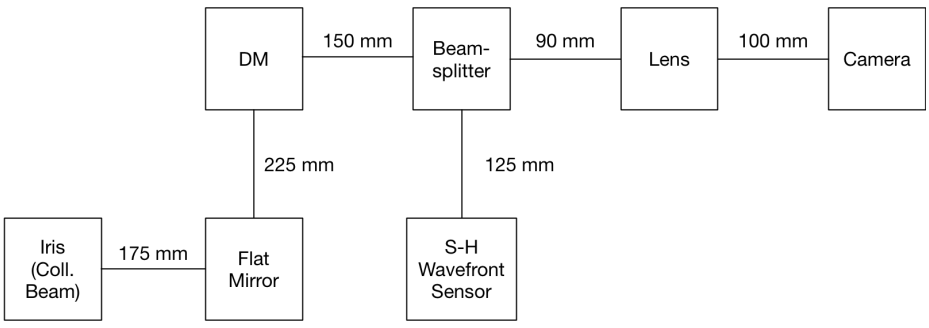

(b)

Figure 3-7: Optical layout of the DeMi payload (a) with camera and lens located below the shown beamsplitter. Some pictured distances not to scale. The lab setup used for wavefront sensor testing (b) differs considerably from this configuration, particularly in the lack of an optical relay for the SHWFS. Refer to Section 3.4.1 for more detail.

reconstruct accurately, and thus results from this test should be applicable to the low spatial frequency requirements of L3-PAY-02 as well.

The test setup is shown in Figure 3-6. The light source for this test is a 0.5 mW single mode fiber laser at the image plane of a Vixen A80Mf refracting telescope used as a collimator and beam expander, shown at the left of the image. The flatness of the resulting wavefront is verified manually with a shear plate. The beam is reduced to the appropriate pupil size with an iris and then directed at a Boston Micromachines Multi-3.5 DM. The reflected beam is then split by a 50:50 beamsplitter and directed to a flight-like image sensor and SHWFS. This DM differs from the flight DM with smaller stroke and actuator pitch. Specifications for both DMs are included in Appendix C.1.1.

To provide initial spot centroid positions for the SHWFS, data is first collected with 0V on all DM actuators. Then an actuator near the center of the DM is chosen and actuated at a chosen voltage, inducing a single poke on the DM surface. SHWFS data is captured five times over the course of 60 seconds. This is repeated for actuator voltages between 0 and 100V at 25V increments. The same procedure is then repeated for a 4×4 region of actuators rather than a single one. Zonal reconstruction is performed using the measured spot fields.

3.4.2 Lab Results

The initial results of this testing are favorable, but more work is needed to develop the algorithm to fully satisfy payload requirements. Examples of reconstructed wavefronts are shown in Figure 3-9. The reconstruction results shown in this section have been divided by 2 to represent a measurement of the DM surface rather than the wavefront surface. The peak actuator displacements for each voltage as measured by the WFS are shown in Figure 3-10. The values represent the difference between the measured flat background and the peak of the reconstructed spike. Results are plotted along with voltage-displacement test data provided by the DM manufacturer. The measured wavefront results were found to be consistently a factor of 2 smaller than expected. This factor is assumed to be a systematic error and has been corrected in the results

shown. The results for a single actuator track closely with the expected displacements (<37 nm difference), while results for the 4 × 4 region differ more, with a maximum error of 120 nm. The standard deviation of each 5-sample actuator measurement is <4 nm for the single-actuator case and <3 nm for the 4 × 4 case.

3.4.3 Lab Test Discussion

The error measured in this experiment is single point, and thus conformance to the 32 nm RMS error requirement in L3-PAY-03 is not verified. However, the maximum single-point error in the single actuator case is 37 nm, whish is on the right order to meet the requirement. The results of the 4 × 4 case are consistently high by approximately 100 nm, but track the shape of the displacement curve. More testing and calibration may eliminate this offset.

The precision of the single-point measurement falls within the 6 nm requirement of L3-PAY-01, interpreting it as a 1σ constraint. This is despite using a 0.5 mW laser compared to the 2.5 mW which will be used in flight. The lab environment also has several potential sources of stray light where the DeMi payload is designed to minimize it. The measurement sample size is small however, and more measurements should be taken across multiple actuators to ensure the results remain consistent.

A potential source of the offset error is the choice of reference for the flat DM background. The large size of the 4 × 4 region of influence distorts the measurable area of the DM, making it difficult to choose a reliable datum.

Attempts to measure actuator voltages of 100 V or more resulted in unusable SHWFS spot fields in both the single and 4x4 case. As shown in Figure 3-8, the steep wavefront slopes result in light being redirected into the lenslets near the peak of the actuator. The spots of neighboring actuators are dimmer as a consequence, and spillover from the bright lenslets corrupts their PSFs, preventing centroiding. The 1500 nm displacement expected for a 4 × 4 region active at 100 V induces a wavefront slope of 0.0017, using the same model as is 3.2.1. A ray hitting a surface with that slope will be displaced. Over the 27.5 cm distance between the DM and SHWFS, the ray is displaced by 458 um. The lenslet pitch is 450 um, so the rays from

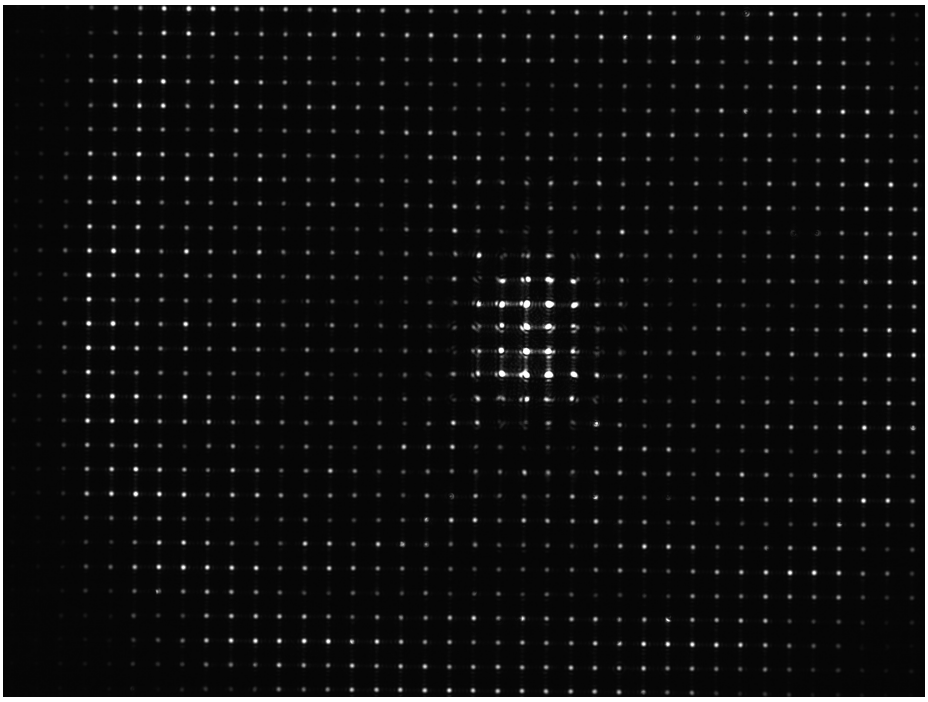

Figure 3-8: Attempts to measure actuator displacements of more than 100 V result in corrupted lenslet spots, preventing reconstruction. This is likely due to the lack of pupil plane conjugation in the lab setup.

part of the pupil with the high slope hit the SHWFS near the center of a neighboring lenslet. The high intensity of the spots in the center of the actuated region in Figure 3-8 clearly shows that the light from neighboring lenslets has been displaced.

Use of an optical relay like in the DeMi payload creates a conjugate plane that has the same intensity and phase as at the pupil plane. The relay reduces the effective distance to zero, so the light from steep DM sections should not reflect into lenslet apertures. Further testing with the DeMi payload or a lab setup including relay optics should be performed to verify that the maximum measurable displacement is not limited by other factors.

As shown in Figure 3-10, the expected displacement of a single actuator at 100 V is 519 nm. A table of voltage-displacement data up to 255 V is included in Appendix C.1.2.

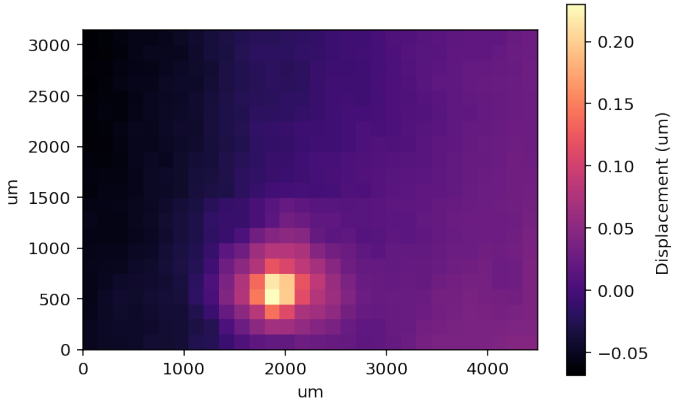

(a)

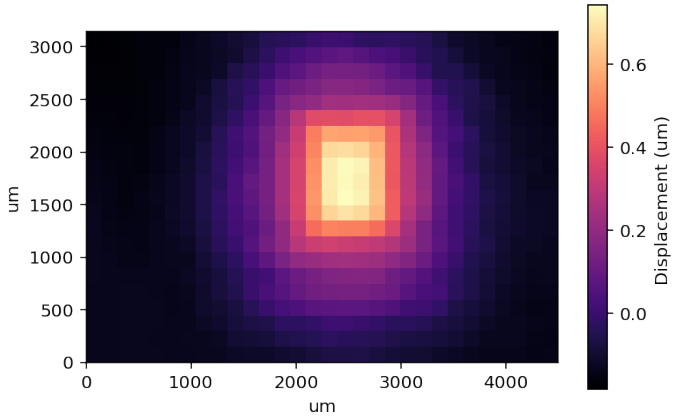

(b)

Figure 3-9: Results of zonal reconstruction from lab data with: a single DM actuator in the lab setup poked at 75V (a); a different 4 by 4 actuator region poked at 75V (b).

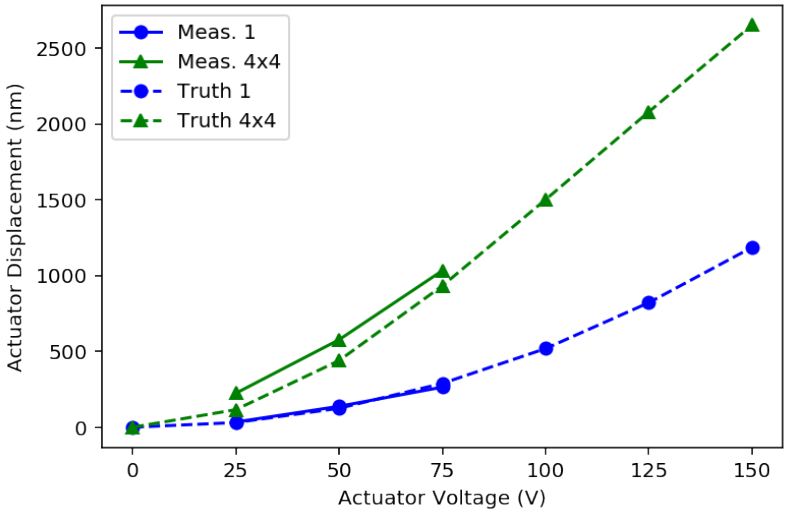

Figure 3-10: Comparison of true DM actuator displacement test data to peak displacements measured by the SHWFS. Results shown for a single actuator poke are marked with circles; results for actuation of a 4×4 region are marked with triangles. The dashed lines represent test data provided by Boston Micromachines and included in Appendix C.1.2. Note that reconstructed wavefronts have been corrected by a factor of 2, which is still unaccounted for.

Chapter 4

Image Plane Wavefront Sensing

In this chapter, we introduce the problem of image plane wavefront sensing in general, using Fourier optics as a mathematical and physical framework. We then discuss the differential optical transfer function (dOTF) method of wavefront sensing. Simulations and experiments are performed in order to asses the viability of the technique for use on DeMi.

4.1 Fourier Optics

Fourier optics is a framework for describing the behavior of optical systems in two dimensions using the language of linear signals and systems. One of the central ideas of this framework is the Fraunhofer approximation, under which a convergent (convex) lens can be seen to behave as a Fourier transform between a pupil plane and an image plane [53]. This behavior is shown in Figure 4-1.

In a simplified optical system, a point source at infinity generates a plane wave $\psi(\boldsymbol{x})$ at a plane in the system called a pupil plane. This field is transformed by the lens to the point spread function (PSF) $\Psi(\boldsymbol{\kappa})$ on the image plane.

$$\Psi(\boldsymbol{\kappa}) = \mathcal{F}[\psi(\boldsymbol{x})] \tag{4.1}$$

Where $\boldsymbol{x}$ is the spatial coordinate on the pupil plane and $\boldsymbol{\kappa}$ is the spatial coordinate on

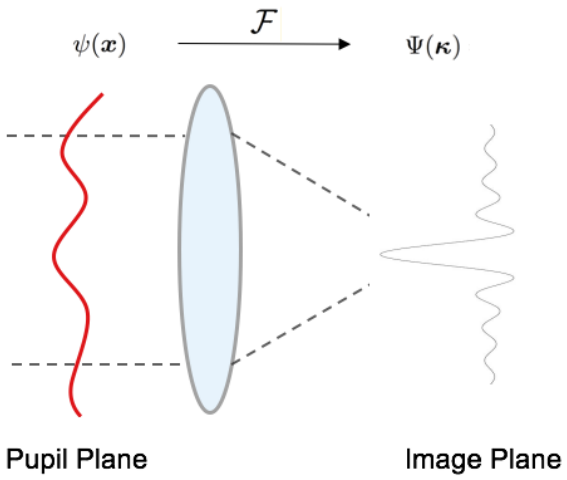

Figure 4-1: Illustration of the Fourier Optics framework.

the image plane. This PSF can be seen as the impulse response of the optical system to the point source at infinity. Here, both the pupil field and PSF are complex such that:

$$\psi(\boldsymbol{x}) = \psi_0(\boldsymbol{x})e^{i\theta(\boldsymbol{x})} \tag{4.2}$$

$$\Psi(\boldsymbol{\kappa}) = \Psi_0(\boldsymbol{\kappa})e^{i\Theta(\boldsymbol{\kappa})} \tag{4.3}$$

Where $\psi_0(\boldsymbol{x})$ and $\Psi_0(\boldsymbol{\kappa})$ are the purely real amplitudes of the pupil and image plane fields, while $\theta(\boldsymbol{x})$ and $\Theta(\boldsymbol{\kappa})$ are their phases.

While we wish to retrieve the phase of $\psi(\boldsymbol{x})$, the constraint is that we can only make measurements in the image plane. In practice the complex-valued field $\Psi(\boldsymbol{\kappa})$ must be measured by a CMOS detector which gives a response proportional to the intensity (squared amplitude) of the field, measuring

$$\Phi(\boldsymbol{\kappa}) = \left|\Psi(\boldsymbol{\kappa})\right|^2 = \left|\mathcal{F}[\psi_0(\boldsymbol{x})e^{i\theta(\boldsymbol{x})}]\right|^2. \tag{4.4}$$

The problem of recovering $\theta(\boldsymbol{x})$ from $\Phi(\boldsymbol{\kappa})$ is broadly called a phase retrieval problem. There are many different techniques to attempt solution of phase retrieval problems, as discussed in Section 2.2.2.

4.2 The Differential Optical Transfer Function (dOTF) Method

The dOTF method [3] solves the phase retrieval problem by making multiple measurements at the pupil plane under different conditions.

By Fourier Optics convention, we define a functional known as the Optical Transfer Function:

$$\mathcal{O}(\boldsymbol{\xi}) = \mathcal{F}^{-1}[\Phi(\boldsymbol{\kappa})], \tag{4.5}$$

which is the autoconvolution of the pupil field:

$$\mathcal{O}(\boldsymbol{\xi}) = \int \psi(\boldsymbol{x}' + \boldsymbol{\xi}/2)\psi^*(\boldsymbol{x}' - \boldsymbol{\xi}/2)\mathrm{d}\boldsymbol{x}'. \tag{4.6}$$

and $\boldsymbol{\xi}$ is a spatial coordinate in the dOTF space, which has been introduced in the convolution.

The dOTF method measures the pupil field $\psi(\boldsymbol{x})$ by approximating of the functional derivative of $\mathcal{O}(\boldsymbol{\xi})$, which is a quadratic functional of $\psi(\boldsymbol{x})$. The derivative of this quadratic functional should be linear in $\psi(\boldsymbol{x})$, so allows it to be easily measured. Approximation of the derivative requires a perturbation be added to the pupil field such that

$$\psi(\boldsymbol{x}) \to \psi(\boldsymbol{x}) + \delta\psi(\boldsymbol{x}). \tag{4.7}$$

This creates a perturbed OTF $\mathcal{O}_{\psi+\delta\psi}(\boldsymbol{\xi})$. Subtracting the original OTF gives the differential optical transfer function (dOTF), which approximates a derivative of the OTF:

$$\begin{aligned} \delta\mathcal{O}(\boldsymbol{\xi}) &= \mathcal{O}_{\psi+\delta\psi}(\boldsymbol{\xi}) - \mathcal{O}_{\psi}(\boldsymbol{\xi}) \\ &= (\psi + \delta\psi) * (\psi + \delta\psi)^* - \psi * \psi^* \\ &= \psi * \delta\psi^* + \delta\psi * \psi^* + \delta\psi * \delta\psi^* \end{aligned} \tag{4.8}$$

The dOTF's three terms can be written as:

$$\delta\mathcal{O}(\boldsymbol{\xi}) = \delta\mathcal{O}_L(\boldsymbol{\xi}) + \delta\mathcal{O}_L^*(-\boldsymbol{\xi}) + \delta\mathcal{O}_{\delta\delta}(\boldsymbol{\xi}) \tag{4.9}$$

where $\delta\mathcal{O}_L(\boldsymbol{\xi})$ is linear in ψ and $\delta\mathcal{O}_{\delta\delta}(\boldsymbol{\xi})$ is quadratic in the perturbation $\delta\psi$. We see that the linear terms are convolutions of the pupil field with the pupil perturbation. It is evident that if the perturbation is spatially compact, these terms simply act as a sampling or sifting of the pupil field such that

$$\delta\mathcal{O}_L(\boldsymbol{\xi}) \approx \psi(\boldsymbol{x}+\boldsymbol{\xi})\mu^* \tag{4.10}$$

where

$$\mu = \int \delta\psi(\boldsymbol{x}')\mathrm{d}\boldsymbol{x}'. \tag{4.11}$$

It can be observed that if the perturbation $\delta\psi$ should be near the edge of the pupil, the three terms in (4.9) are spatially distinct over the domain $\boldsymbol{\xi}$. These terms are the convolved pupil field, its reflection, and the second-order perturbation term. Their locations can be seen in Figure 4-2.

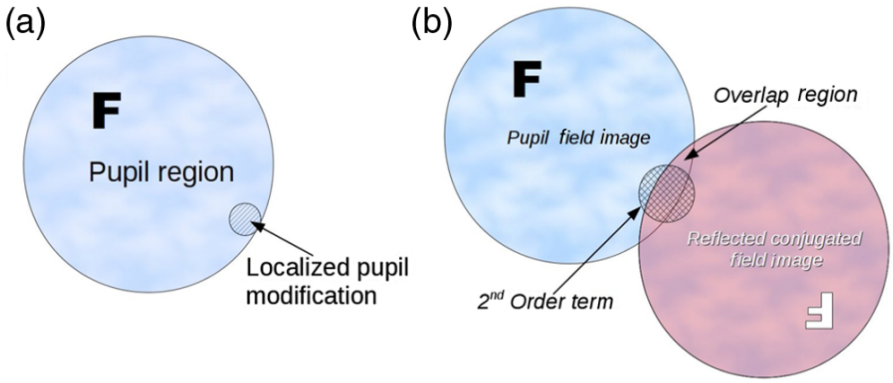

Figure 4-2: Illustration of the spatial distribution of the three terms of the dOTF. [3]

4.3 dOTF Simulation

In order to test the effectiveness of the dOTF algorithm in a context similar to DeMi, an optical system is simulated. The system model consists of a flat wavefront at a wavelength of $\lambda = 675$ nm interacting with an amplitude and phase screen representing a circular aperture and a DM, respectively. The phase screen is set as a

DM with several of the actuators poked at $\sim \lambda/4$ displacement. The resulting ground truth pupil field $\psi_t(\boldsymbol{x})$ is shown in Figure 4-3a and 4-3b. Then, the measured intensity $\Phi_m(\boldsymbol{\kappa})$ of the PSF generated by the pupil field as viewed through a converging lens is simulated via Fraunhofer Diffraction using POPPY [52].

An additional pupil and image plane signal are then simulated, where the phase screen has an additional DM actuator engaged, acting as the perturbation $\delta\psi$, shown in Figure 4-3c. The dOTF $\delta\mathcal{O}_L(\boldsymbol{\xi})$ is then calculated from the two images, as shown in Figure 4-4. We see that the signal is recognizable, but additional processing is required in order to estimate the pupil field.

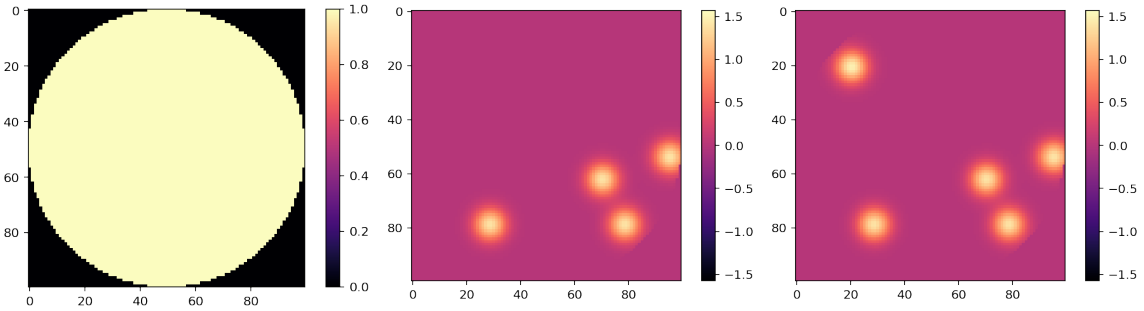

(a) (b) (c)

Figure 4-3: Setup for the numerical simulation with the dOTF algorithm. The ground-truth amplitude (a) and phase (b) in the pupil plane are shown. An additional pupil perturbation is added in (c). The spatial axes are given in pixels and the color scale is in radians of wavefront phase.

One difficulty with the dOTF results is that the translation between the dOTF coordinates and the pupil coordinates depends on the location of the pupil perturbation. In order to compare with the truth phase, the proper translation must be computed. For the purposes of interpreting the this simulation, a best-fit translation to the ground truth phase is calculated. In a practical scenario the truth phase is not known, so a different technique will have to be used. Discussion of this problem can be found in Section 5.1.2. The results are then masked to exclude the quadratic perturbation term, and are compared with the ground truth.

The results are shown in Figure 4-5. We see that the phase is reconstructed well overall, as the actuators are visible. The error shown in Figure 4-5c indicates that the

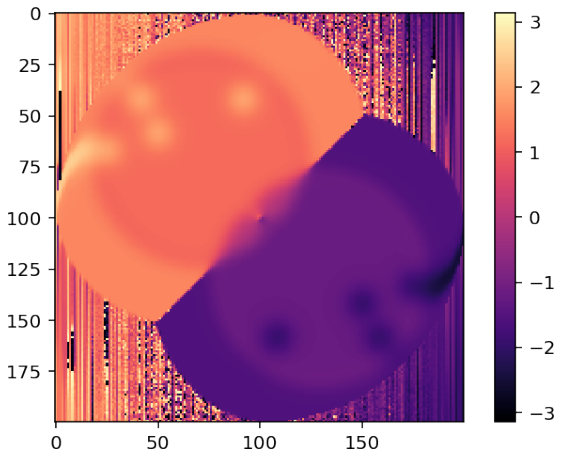

Figure 4-4: Unprocessed, simulated dOTF result, showing the two linear terms of the dOTF are spatially distinct except for overlap at the point of the pupil perturbation. Four actuators are displaced by $\lambda/4$, plus an additional actuator as the dOTF phase perturbation. The expected pupil phase is visible in each term. The spatial axes are given in pixels and the color scale is in radians of wavefront phase.

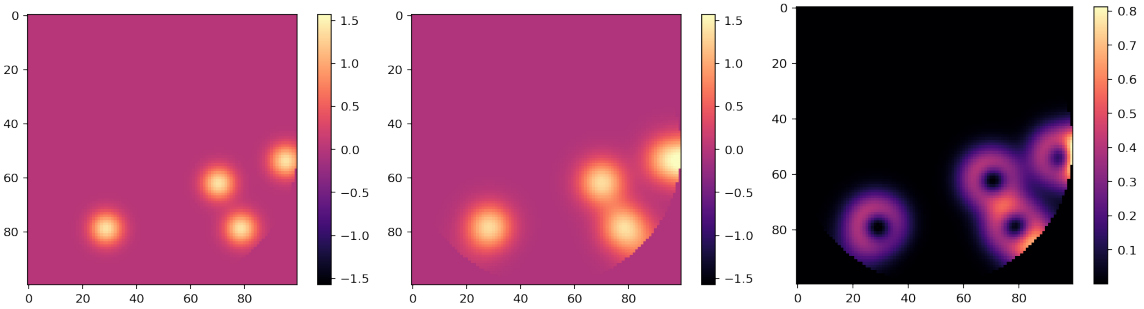

(a) (b) (c)

Figure 4-5: Results of the simulation of the dOTF method. The ground-truth phase is in (a) and the reconstructed phase is shown in (b). The masked error between truth and reconstruction is shown in (c). The spatial axes are given in pixels and the color scale is in radians of wavefront phase.

reconstructed actuator pokes are of roughly the correct magnitude and there are no background artifacts. However, the image is blurred with the residuals appearing as a ring around each actuator location. This is because the results are convolved with the influence function of actuator used as the perturbation $\delta\psi$.

In this experiment, the maximum phase error at the peak of any actuator is 35 mrad. At the simulated wavelength, this is 3.76 nm phase error, or 1.8 nm surface error on the DM. The overall RMS phase error between the true and reconstructed

phase is 135.6 mrad, while the maximum absolute phase error is 812.7 mrad. The RMS phase error translates to an RM surface error of 7.3 nm. This satisfies L3-PAY-03 with an RMS surface measurement error <32 nm.

This simulation is performed with noiseless conditions, so precision cannot be determined and additional simulation and testing is required to determine the effect of image sensor read noise. The largest source of measurement error that is present blurring of the actuators by convolution with the pupil perturbation. Potential deconvolution methods are discussed in Section 5.1.2.

4.4 Lab Results

To test the dOTF method in the presence of noise, imperfect optical alignment, and other potential sources of error, a lab setup is constructed as described in Section 3.4. In order to make a single dOTF measurement, two different images are taken. For the first image, a single DM actuator near the center of the DM is actuated with 75 V and the resulting PSF is captured. In the second image that actuator is kept at 75V while another near the edge is actuated to the same level. The second actuator acts as the pupil perturbation that supplies the necessary phase diversity for the measurement.

To provide a baseline wavefront measurement for the relaxed DM surface, an additional pair of images is taken. The first measures the PSF with all actuators at 0 V, while the second measures the PSF with the same edge actuator active as before. The dOTF result is wrapped modulo 2π, so a 2D phase unwrapping algorithm [54] is applied. The dOTF of the baseline wavefront (Fig. 4-6b) is subtracted from the dOTF with the actuator poke (Fig. 4-6c).

The resulting wavefront is cropped and shown in Figure 4-7. The magnitude of this wavefront displacement is 1176 nm, or 588 nm DM surface displacement. The expected displacement for a single actuator at 75V on this DM is 289 nm. This is approximately a factor of two higher than expected. More data is needed to determine the source of this error. DM voltage-displacement data can be found in Appendix C.1.2.

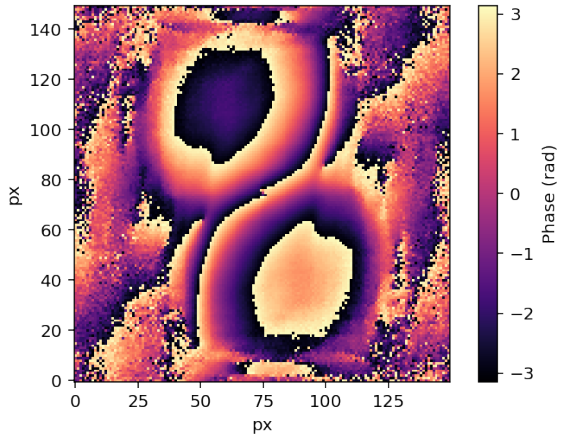

(a)

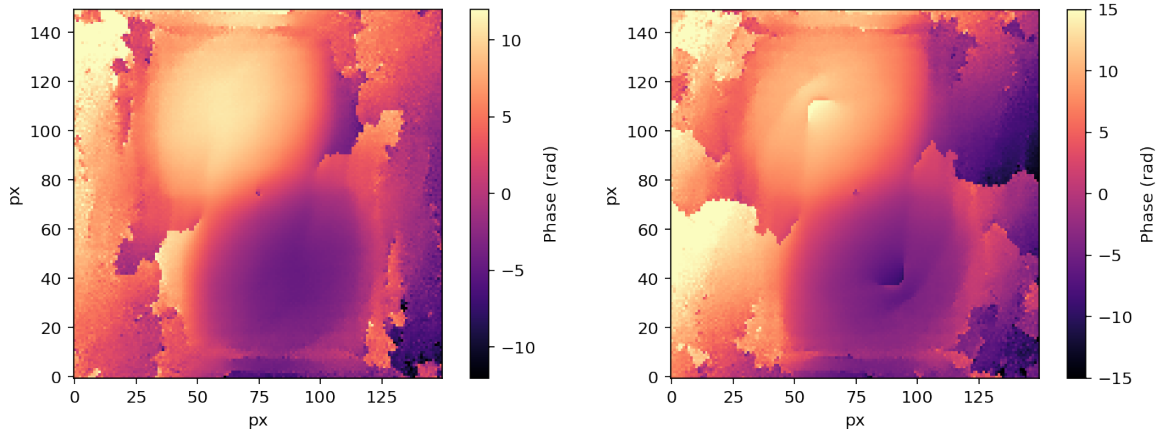

(b) (c)

Figure 4-6: dOTFs from laboratory data. These measurements show the relaxed DM surface (a) before and (b) after unwrapping. (c) shows measurement of the DM surface with a single actuator poke present.

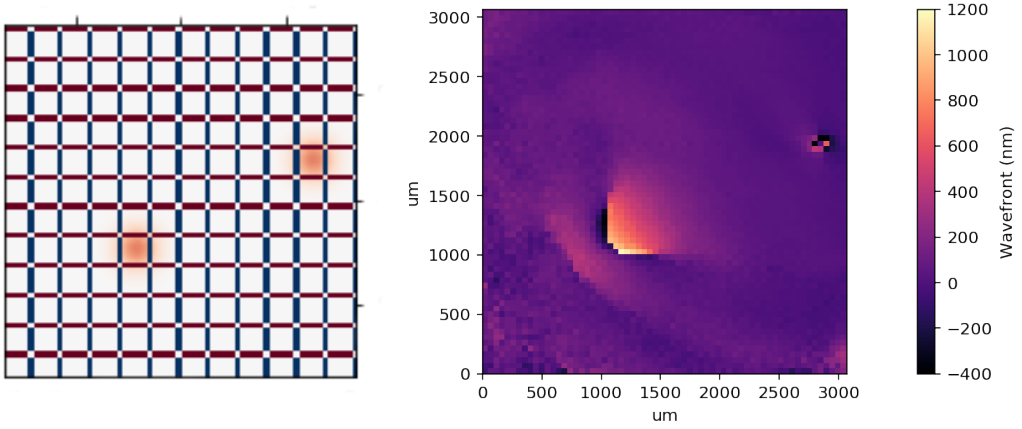

(a) (b)

Figure 4-7: The two actuators active on the DM (A) in the lab test. The one at the right edge is used to provide phase diversity for the dOTF measurement. Two images are used to perform a dOTF reconstruction. The cropped result (b) with background curvature subtracted, clearly shows the actuator poke near the DM center.

Chapter 5

Calibration, Validation, and Future Work

The evaluations of the dOTF and SHWFS zonal reconstruction methods in this thesis are positive, but preliminary. This chapter discusses steps that remain to enable the use of zonal reconstruction and the dOTF on the DeMi mission. Section 5.1 suggests calibration methods for both techniques to improve accuracy. Section 5.2 evaluates the ability of the dOTF and SHWFS to satisfy the requirements based on the results of the investigations in this thesis. Section 5.3 suggests concrete steps that can be taken to improve, and validate these wavefront sensing methods and integrate them into the DeMi mission.

5.1 Calibration

This section describes methods that could be used to improve the performance of the SHWFS and dOTF wavefront sensing methods. The focus is on the determination of mechanical and optical parameters that affect wavefront sensing results and obscure the measurement of the DM surface. These procedures calibrate the DeMi payload instrument as a whole, and so operations involving both the SHWFS and dOTF are discussed.

5.1.1 SHWFS Parameter Calibration

The zonal reconstruction methods discussed in Section 3.1 rely on knowledge of the mechanical parameters of the SHWFS system. Specifically, P, the lenslet pitch, S, the pixel size, and f, the focal length all must be accurately known. For example, an error in focal length has a proportional effect on the error in the measured wavefront such that:

$$\delta\psi = \frac{\delta f}{f_0 + \delta f}\psi_0 \tag{5.1}$$

where $\delta\psi$ is the error in the wavefront, δf is the error in the focal length, f_0 is the true focal length, and ψ_0 is the true wavefront [55]. The observed effective focal length of the DeMi lenslet array is $f_0 = 5.1$ mm as shown in Table 3.1. This differs from the specified focal length of 5.2 mm, so it is reasonable to assume that $\delta f \leq 0.1$ mm. With these values and Equation 5.1, we can predict a $\leq 1.9\%$ error in measured wavefront. Over the full stroke of 5.5 um, this would result in an error of up to 106 nm.

Wavefront reconstruction errors can be reduced through the use of calibration techniques to determine the true values of SHWFS parameters. A common technique uses a SMF as a source of a spherical wavefront for use as a calibration source. This arrangement is shown in Figure 5-1. Chernyshov et al. suggest using the SHWFS to measure the radius R of the wavefront curvature at several distances [56] . A variable $\rho = 1/R$ can be introduced. The error $\delta\rho$ between the measured and true wavefront curvature can be plotted as a function of the true wavefront curvature. The value of true wavefront radius of curvature is determined by measuring distance to a reference point on the SHWFS, giving a value of ρ_{ref} at each distance. A polynomial can be fit to the $\delta\rho$ vs. ρ_{ref} plot. Its coefficients can be compared with the following relation to give estimates for the parameters:

$$\delta\rho = \rho_{ref}^2\delta R - \rho_{ref}\frac{\delta f}{f_0} - \frac{1}{f_0}\left(\frac{\delta P}{P_0} - \frac{\delta S}{S_0}\right) \tag{5.2}$$

Where δP , δS , and δf are the errors between the true parameter values and the

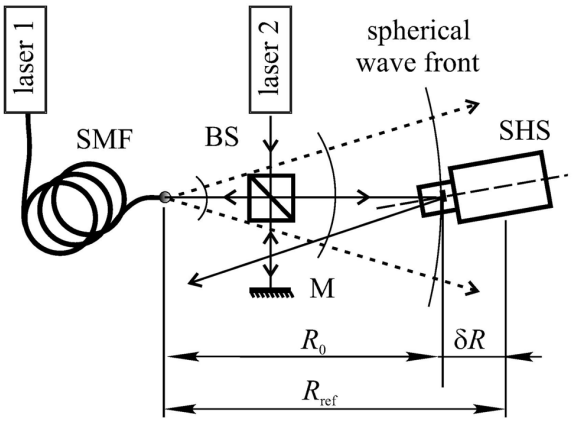

Figure 5-1: Example of a setup used to calibrate the SHWFS mechanical parameters using a single-mode fiber (SMF) as the source of a spherical wave. An additional collimated laser is used to ensure alignment between the spherical wave and the SHWFS. [56]

nominal values P_0 , S_0 , and f_0. δR is the offset between the reference point on the SHWFS used for curvature radius measurement and the true location of the lenslet array. One difficulty with this technique is the need for an accurate curvature radius measurement. Yang et al. suggest a modified technique where the majority of the error is assumed to come from the error in f [55]. An initial focal length estimate can first be obtained by assuming the other parameters at their nominal values. These values can then be refined using a modified form of Equation 5.2.

$$\delta\rho = \rho_{ref}^2 \delta R - \frac{1}{f_0}\left(\frac{\delta P}{P_0} - \frac{\delta S}{S_0}\right) \tag{5.3}$$

SHWFS parameter calibration should be performed before the sensor is installed in the payload. After installation, additional calibration is needed to compute corrections for factors external to the SHWFS. This is discussed in Section 5.1.3.

5.1.2 dOTF Mapping and Deconvolution

A major challenge with the dOTF method is that the results are given in the dOTF coordinate space shown in Figure 4-2 rather than spatial coordinates in the pupil plane. The transformation between this dOTF space and pupil coordinates is non trivial because it is dependent on the position of the pupil modification, and the pupil

size in angle space is not exactly known. The mapping between the dOTF space and pupil space can be determined experimentally by poking individual actuators in a test pattern as described in [57]. Two dOTF measurements are needed to cover the whole pupil because each has an obscuration in the area near the pupil perturbation. The mapping must therefore be done twice, performing dOTFs with each of the two chosen pupil modification actuators. The mapping between dOTF coordinates and pupil coordinates can be used to synthesize two dOTF measurements into a single pupil plane measurement of the DM surface.

The dOTF results differ from the actual phase because the result is convolved with the influence function of the actuator. If high-resolution wavefront measurements are desired, the theoretical influence function can be used as a deconvolution kernel as described in [58].

5.1.3 Optical Path Aberrations

Once the SHWFS itself is calibrated, we must determine the wavefront error imparted by imperfections in the relay optics between it and the DM. When the internal SMF source is used it adds a spherical wavefront contribution, and the DM itself has a curved surface when un-powered and so adds its own low-order aberrations. The sum of all these aberrations is treated as a reference flat wavefront which all future wavefront measurements are compared to. It can be incorporated into wavefront sensing by storing the locations of the SHWFS lenslet spots as reference locations as described in Section 3.1.1. Alternatively, a pre-existing map of reference spots can be used for a wavefront measurement and the reconstructed reference wavefront can be stored for subtraction from future measurements.

When light from the external aperture is used for DM measurement, the shape of the wavefront hitting the DM is be nearly flat rather than spherical. Wavefront aberrations from imperfections and misalignments in the optical path between the aperture and the DM are also be present. Since this wavefront is different from that observed when using the internal source it is necessary to repeat the above calibration process using a collimated light source in payloadâĂŹs external aperture.

The approach of observing wavefronts with the DM un-powered can also be used to determine static wavefront aberrations at the image plane. Two dOTF measurements with different perturbation actuators can be taken and combined into a complete pupil measurement. This background wavefront can be subtracted from dOTF measurements of the DM. A similar approach was taken to calculate the final dOTF lab results in Section 4.4. The dOTF background wavefront measurements can be compared with the SHWFS measurements to determine wavefront differences between the two sensors.

The difference between aberrations in the two optical paths is potentially useful in accounting for non-common-path errors when attempting wavefront control. A correction can be applied to SHWFS output before it is used to calculate DM displacements. In order to apply image-plane data to the dOTF, a mapping would have to be computed between the SHWFS and dOTF spaces. The method used in Section 5.1.2 could potentially be adapted for this purpose.

5.1.4 On-orbit Calibration

There is likely to be some displacement of optical elements due to the vibration and shock conditions during launch and deployment. Once DeMi is in orbit and the spacecraft systems are commissioned, any aberrations induced by this shifting can be determined and compensated. For this purpose, the same procedure used for calibration on the ground can be repeated: wavefront measurements can be taken using both wavefront sensing methods with the internal light source. When a suitable stellar target is chosen, the new reference measurement can be chosen using that as a source. However, spacecraft actuator disturbances could prevent a clean reference measurement with a stellar source. The pre-launch external reference can be used on orbit, but it will not capture launch-induced misalignments. A SHWFS reference with unknown errors is problematic because it will impair the wavefront control system's ability to flatten the wavefront.

Comparing the on-orbit reference wavefront from the internal source with the pre-launch internal-source reference should reveal any launch-induced aberrations in

the optical paths downstream of the SMF. If the change in aberrations is small, this may indicate that the pre-launch external-source reference can be used for wavefront sensing and control, but unseen misalignments in the optical path may still exist upstream of the field mirror and SMF. The measurement of reference wavefronts can be repeated throughout the mission to identify and correct any additional changes due to thermal expansion.

5.2 Validation

In this section we discuss validation of the DeMi Payload's ability to meet the payload, science, and ultimately the mission requirements.

5.2.1 SHWFS Validation

The Simulation of SHWFS operation in Section 3.3 demonstrates that the chosen zonal reconstruction algorithm is capable of satisfying the 32 nm RMS accuracy requirement of L3-PAY-03 over more than the 5.5 um DM stroke, with Zernike modes of higher order than the required tilt, focus, astigmatism, coma, and spherical.

The lab tests validate that the methods can be implemented on flight-like hardware in a real optical system. They also show that the SHWFS can meet the 6 nm precision requirements of L3-PAY-01 and L3-PAY-03 despite having a lower laser source brightness and a lab environment with sources of stray light. Additionally, analysis by Douglas [26] indicates that the DeMi SHWFS should be capable of meeting wavefront error requirements when using bright stellar sources.

Lab accuracy measurements do not yield surface RMS values, but point errors values of less than 150 nm prior to performing the calibration discussed in Section 5.1.1 increase confidence that the simulation is valid and that the RMS accuracy requirement can be met in practice. The lab tests are not able to measure the full displacement of the DM actuators, but this is likely due to the difference between the lab setup and flight optical configuration. The simulation and the analysis in Section 3.2.1 show that the system should be able to meet this requirement. To complete

validation of the SHWFS, the lab tests should be repeated in a more representative optical system. Ideally, the completed DeMi optical payload should be used for testing.

5.2.2 dOTF Validation

The SHWFS alone should be able to meet the requirements of the DeMi mission, but the additional dOTF technique provides failure tolerance and fulfills L1-MIS-04, testing different wavefront sensing algorithms.

Similarly to the SHWFS methods, the dOTF's RMS accuracy is validated by simulation, with very low surface error under 2 nm. Deconvolution could improve these results even further. However, the dOTF's ability to measure displacements up to the DM stroke has not been determined. Lab testing confirms the basic operation of the dOTF method, but does not provide information about the precision of the technique and does not reach full-stroke displacement.

The dOTF is promising, but additional simulations with higher actuator displacements should be performed, and more lab data should be collected in order to estimate precision.

5.3 Future Work

5.3.1 Wavefront Sensing

Additional testing is required to validate that the SHWFS and dOTF are suitable for use on DeMi, and to integrate the techniques with the DeMi payload hardware and software.

SHWFS Improvements

- The factor of two error in the SHWFS lab results should be found in order to verify that it is indeed systematic. The error does not appear in the simulations, so it is likely a mismatch between the physical parameters of the SHWFS and

those used in the reconstruction. Parameters should be checked carefully, and the simulation should be validated as described below.

- Tests should be performed on a more representative optical system with a pupil relay, or on actual DeMi optical hardware, to verify that the non-uniform illumination and malformed spots seen in Figure 3-8 are a result of the lab setup and do not occur. The results of testing with a more flight-like system will be more directly applicable to the DeMi payload, so all lab testing performed should be repeated with it.

- SHWFS testing should be performed with the DM which has been calibrated by BMC. This will allow actuation of Zernike modes, which can be replicated in the SHWFS simulation. Slope data form the real sensor can be compared with simulated slope data from the simulated wavefront in order to validate the simulated SHWFS.

- Different centroid methods should be explored to optimize the performance of the DM and allow operation with dimmer stellar targets. Nightingale and Gordeyev discuss methods such as thresholding and gamma correction that can be applied to improve the performance of the center-of-mass method and others [46].

dOTF Improvements

- dOTF simulation should be performed with higher DM actuations. More dOTF lab testing should be done so the precision can be determined. Use of the dOTF on orbit also depends on the performance of mapping etween the dOTF and pupil plane. The mapping technique in Section 5.1.2 should be implemented and tested.

- dOTF results also had to be corrected by a factor of two. In this case, the results were higher than expected, but performance was consistent once the correction

was made. The software implementation of the dOTF should be checked for errors against the dOTF formulation.

5.3.2 Flight Software Implementation

Due to limitations on the volume of data stored on board the DeMi spacecraft and downlinked during limited radio contacts, full-frame SHWFS images for each measurement should not be stored. Instead, data processing should be done on board to reduce the images to an array of spot positions or displacements. Actual wavefront reconstruction can potentially also be performed on board in order to enable quicker identification of any issues with the DM. To implement these features will require rewriting the Python implementations of the wavefront sensing algorithms in C++.

Analysis is required to determine if dOTF calculations can be performed on board the spacecraft. Two Fourier transforms must be calculated for each dOTF. If 140 actuators and 9 regions of 4×4 are each measured at 10 voltages, then 1490 dOTFs must be computed. The DeMi payload computers should be benchmarked to determine computation time for this number of dOTFs. Alternatively, PSFs can be captured and stored for each DM poke during open-loop testing described in Section 2.3. Each dOTF tequires two PSFs per measurement. If these images are to be stored and downlinked: 500×500 trimmed PSF image are about 250kB when stored as uncompressed binary data. Each dOTF requires tewo of these images, for 500kB per dOTF. Every set of 1490 DM measurements would be 745 MB, which is likely too large to store and downlink regularly even for a 1 Mbps link. The images are likely to be compressible, so lossless compression methods should be investigated.

5.3.3 Implementing Calibration

The calibration techniques outlined in Section 5.1 have not yet been implemented and tested for the DeMi mission. The SHWFS parameter calibration requires the setup of the calibration source as pictured in Figure 5-1. Analysis code should to be written to determine wavefront curvature and calculate best-fit of the parameters.

Appendix A

The Gerchberg-Saxton Algorithm

The Gerchberg-Saxton Algorithm [41, 40] is a classic approach to phase retrieval, where the signal is iteratively transformed between the image and pupil planes and constraints are repeatedly imposed on the signal in each domain.

A.1 Theory

The algorithm is performed with the following operations at each step k. We see that each iteration requires one forward and one inverse Discrete Fourier Transform operation.

$$\Psi_k(\boldsymbol{\kappa}) = \left|\Psi_k(\boldsymbol{\kappa})\right| e^{i\Theta_k(\boldsymbol{\kappa})} \leftarrow \mathcal{F}[\psi_k(\boldsymbol{x})] \tag{A.1}$$

$$\Psi'_k(\boldsymbol{\kappa}) \leftarrow \left|P(\boldsymbol{\kappa})\right| e^{i\Theta_k(\boldsymbol{\kappa})} \tag{A.2}$$

$$\psi'_k(\boldsymbol{x}) = \left|\psi'_k(\boldsymbol{x})\right| e^{i\theta'_k(\boldsymbol{x})} \leftarrow \mathcal{F}^{-1}[\Psi'_k(\boldsymbol{\kappa})] \tag{A.3}$$

$$\psi_{k+1}(\boldsymbol{x}) = \left|\psi_{k+1}(\boldsymbol{x})\right| e^{i\theta_{k+1}(\boldsymbol{x})} \leftarrow \left|p(\boldsymbol{x})\right| e^{i\theta'_k(\boldsymbol{x})} \tag{A.4}$$

The constraints in each domain are here applied to the amplitudes of the signals, and are represented by $\left|P(\boldsymbol{\kappa})\right|$ and $\left|p(\boldsymbol{x})\right|$ in the image and pupil planes, respectively. The measured data about the wavefront in question enters through one or both of these terms. The terms may also be determined by assumptions about problem geometry.

The behavior of the algorithm can be shown as follows. We represent the mean

squared error in $\Psi_k(\boldsymbol{\kappa})$ at each step k as

$$E_{\Psi k}^2 = N^{-2} \sum_{\boldsymbol{\kappa}} \left| \Psi_k(\boldsymbol{\kappa}) - \Psi_k'(\boldsymbol{\kappa}) \right|^2 \tag{A.5}$$

where N is the number of pixels in each spatial dimension. We can then see by Parseval's theorem that

$$E_{\Psi k}^2 = N^{-2} \sum_{\boldsymbol{\kappa}} \left| \Psi_k(\boldsymbol{\kappa}) - \Psi_k'(\boldsymbol{\kappa}) \right|^2 = \sum_{x} \left| \psi_k(\boldsymbol{x}) - \psi_k'(\boldsymbol{x}) \right|^2 \tag{A.6}$$

and we define the error term in the pupil plane slightly differently.

$$E_{\psi k}^2 = \sum_{x} \left| \psi_{k+1}(\boldsymbol{x}) - \psi_k'(\boldsymbol{x}) \right|^2 \tag{A.7}$$

We can observe that (A.7) and (A.6) can be related by

$$\left| \psi_{k+1}(\boldsymbol{x}) - \psi_k'(\boldsymbol{x}) \right| \leq \left| \psi_k(\boldsymbol{x}) - \psi_k'(\boldsymbol{x}) \right| \tag{A.8}$$

because $\psi_{k+1}(\boldsymbol{x})$ and $\psi_{k+1}(\boldsymbol{x})$ have the same amplitude, namely $\left|p(\boldsymbol{x})\right|$, but by definition, $\psi_{k+1}(\boldsymbol{x})$ is closer in phase to $\psi_k'(\boldsymbol{x})$. Therefore, we see that

$$E_{\psi k}^2 \leq E_{\Psi k}^2 \tag{A.9}$$

Similarly, we can show that

$$\left| \Psi_{k+1}(\boldsymbol{x}) - \Psi_{k+1}'(\boldsymbol{x}) \right| \leq \left| \Psi_{k+1}(\boldsymbol{x}) - \Psi_k'(\boldsymbol{x}) \right| \tag{A.10}$$

and again using Parseval's theorem

$$E_{\Psi k+1}^2 \leq E_{\psi k}^2 \leq E_{\Psi k}^2 \tag{A.11}$$

such that the data misfit must decrease or remain constant with each iteration [40]. However, the step of enforcing the amplitude constraints can be seen as a projection

onto a non-convex set, and as such a proof of actual convergence of the algorithm has not been found [59].

A.2 Simulation

In order to test the efficacy of the Gerchberg-Saxton algorithm for phase retrieval as applicable to the DeMi satellite payload, a sample optical system was simulated. The system consisted of a flat wavefront at a wavelength of $\lambda = 675$nm interacting with an amplitude and phase screen representing a circular aperture and a DM, respectively. The phase screen was set as a DM with several of the actuators "poked" at $\sim \lambda/4$ displacement. The resulting ground truth pupil field $\psi_t(\boldsymbol{x})$ is shown in Figure **??** and 4-3a. Then, the measured intensity $\Phi_m(\boldsymbol{\kappa})$ of the PSF generated by the pupil field as viewed through a converging lens was simulated via Fraunhofer Diffraction (Figure A-1).

The Gerchberg-Saxton algorithm was run for 1000 iterations with

$$\big|P(\boldsymbol{\kappa})\big| = \sqrt{\Phi_m(\boldsymbol{\kappa})} \tag{A.12}$$

$$\big|p(\boldsymbol{x})\big| = \big|\psi_t(\boldsymbol{x})\big| \tag{A.13}$$

as generated by the simulation. We note that the latter of these values is a quantity that might not be measured exactly in an actual lab setting. Namely, the shape of the aperture might not be exactly known.

The results of the experiment are shown in Figure A-2. We see that the features of the DM actuators are reconstructed well, though there is a symmetrical error in the wavefront. Using a binary mask in the shape of the aperture, the error was measured across the area of the pupil with non-zero field amplitude. The RMS error in the masked reconstruction was 155.6 mrad, while the maximum absolute error was 841.9 mrad.

The convergence of the algorithm was tracked via the data misfit. Specifically, the RMS amplitude error of the in the image plane is shown in Figure A-3. The

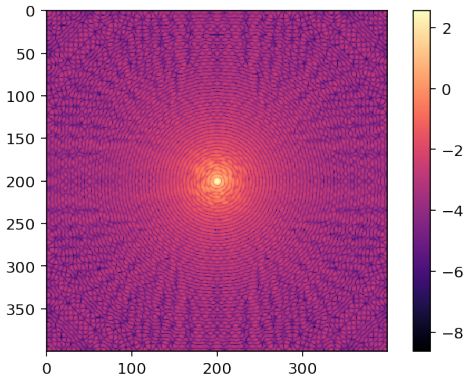

Figure A-1: Logarithm of simulated PSF intensity as generated by the test pupil field.

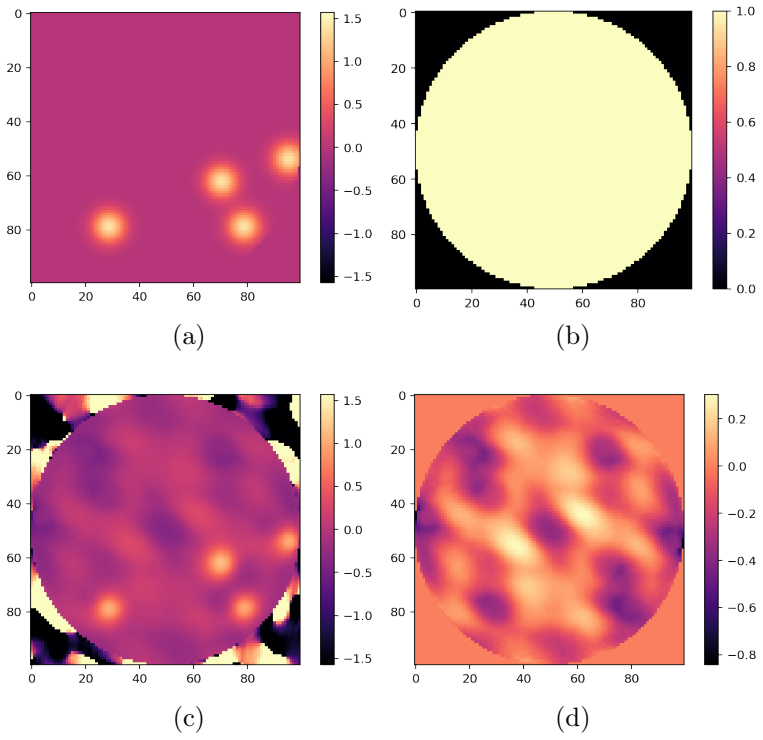

Figure A-2: Setup and results of the numerical experiment with the Gerchberg-Saxton algorithm. The ground-truth phase (a) and amplitude (b) in the pupil plane are shown. The reconstructed phase is shown in (c). The masked error between truth and reconstruction is shown in (d), with a different color scale.

algorithm can be seen to plateau for many iterations and then continue to converge before plateauing again. It is possible that more iterations would result in a better reconstruction.

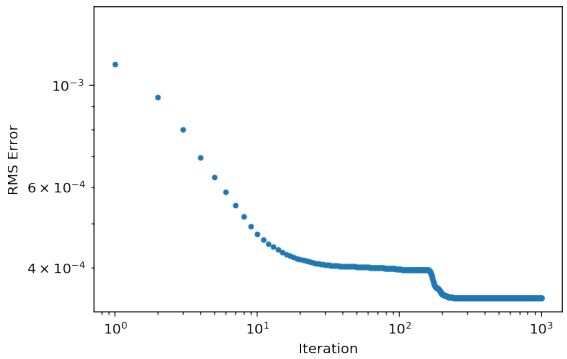

Figure A-3: Convergence of the data misfit in the Gerchberg-Saxton Algorithm.

Appendix B

Original Requirements

Some requirements as written in the DeMi System Requirements Review (SRR) documentation are out of date or unclear. The versions included in the preceeding text are revised, and the original versions are included here.

Designator	Description	Requirement
L1-MIS-01	DM Operation in Space	DeMi shall demonstrate the operation of a MEMS deformable mirror in space.
L1-MIS-02	Wavefront Correction in Space	DeMi shall measure and correct wavefront phase aberrations in space.
L1-MIS-03	Observe Stars	DeMi shall measure stellar point spread functions and photometric intensities.
L1-MIS-04	Wavefront Sensing Algorithms	DeMi shall enable testing and improvement of wavefront sensing algorithms on orbit.
L1-MIS-05	CubeSat	DeMi shall be built in accordance with the standard CubeSat architecture.

Table B.1: Original DeMi Mission Requirements

Requirement L1-MIS-04 is revised to read "DeMi shall enable testing and improvement of wavefront sensing algorithms on orbit." This is more appropriate for a top level mission requirement, as its broader and can be flowed to various subsystems. It is also more informative about the rationale behind requiring on-orbit software updates.

Requirement L3-PAY-02, L3-PAY-03, L2-SCI-04, and L2-SCI-05 are updated to

Designator	Description	Requirement
L2-SCI-01	Measure Displacement	The payload shall measure individual deformable mirror actuator wavefront displacement contributions to a precision of 12nm.
L2-SCI-02	Measure Low Order Modes	The payload shall measure low order aberrations to $\lambda/10$ accuracy and $\lambda/50$ precision.
L2-SCI-04	Static WFE correction	The payload shall correct static wavefront phase errors up to the DM Nyquist spatial frequency with magnitudes below 3.5microns to less than 100nm RMS.
L2-SCI-05	Dynamic WFE Correction	The payload shall correct dynamic wavefront phase errors up to the DM Nyquist spatial frequency with magnitudes up to 3.5 um to less than 100nm RMS.

Table B.2: Original DeMi Science Requirements

Designator	Description	Requirement
L3-PAY-01	Measurement Accuracy	The payload wavefront sensor shall measure wavefront phase errors up to the DM Nyquist spatial frequency with magnitudes below 3.5 microns (TBR) surface error to less than 6 nm RMS surface error (TBR).
L3-PAY-02	Correction Accuracy	The payload shall correct static wavefront phase errors up to the DM Nyquist spatial frequency with magnitudes below 3.5 microns (TBR) to less than 100 nm RMS (TBR).
L3-PAY-03	Measure Zernikes	The WFS shall measure the internal RMS surface error due to tilt, focus, astigmatism, coma, and spherical aberration to 32 nm (TBR) accuracy with 6 nm precision (TBR).
L3-PAY-05	Speed	The payload shall perform wavefront error measurement and apply corrections to the DM surface in a closed loop at at 12 Hz (TBR) or faster.
L3-PAY-09	Centroiding	The payload wavefront sensor detector shall permit PSF centroiding to 0.01 pixels using the internal laser source.

Table B.3: Original DeMi Payload Requirements

read "up to the spatial frequency and stroke capabilities of th DM" rather than calling for measurement or control at both maximum stroke and Nyquist frequency simultaneously. The DM cannot actuate to that maximum stroke at the DM Nyquist

frequency, so there is no need to measure that condition. The DM Nyquist frequency is usually defined as that with 2 actuators per wave, and is the highest spatial frequency that can be induced by the DM.

$$f_{Ny} = \frac{N}{2D} \quad [m^{-1}] \tag{B.1}$$

The max displacement is only reached when actuating a 4 x 4 actuator region at maximum voltage, which corresponds to the spatial frequency with 8 actuators per wave. The intent of L3-PAY-02 is to be able to measure the DM in any actuation condition, with the most difficult likely a 4 x 4 DM poke at max displacement.

L3-PAY-02 is also edited to clarify that the requirement is on precision rather than accuracy.

These changes will be reviewed and then incorporated into the formal DeMi requirements documents.

Appendix C

Data Sheets

C.1 DM Data

C.1.1 DM Specifications

The following chart shows specifications for Boston Micromachines Low-actuator DMs. The DeMi flight payload uses the Mini-5.5, while the Mini-3.3 is used for experiments in this thesis.

DM Specifications*	Total Actuator Count	Actuator Count Across Aperture	Stroke (μm)	Aperture (mm)	Pitch (μm)	Mechanical Response (10% - 90%)	Approximate Interactuator Coupling	Price**
Ultra-Compact Mini-1.5	25	5	1.5	1.2	300	<40 μs	15%	$7,000
Mini-3.5	32	6	3.5	2.0	400	<75 μs	13%	$7,500
Mini-5.5	32	6	5.5	2.25	450	<100 μs	22%	$12,500
Multi-C-1.5	137	13	1.5	3.6	300	<40 μs	15%	$12,000
Multi-3.5	140	12	3.5	4.4	400	<75 μs	13%	$17,900
Multi-5.5	140	12	5.5	4.95	450	<100 μs	22%	*Upon Request*
Multi-SLM†	140	12	1.5	3.6	300	<35 μs	0%	*Upon Request*

†Segmented surface mirror. All other configurations have continuous surfaces.
*High speed driver options are available.

**Includes mirror, driver and operational software

C.1.2 Mini-3.5 Voltage-Displacement Data

The following is manufacturer-provided test data from the Boston Micromachines Multi-3.5 DM unit used for experiments in this thesis.

BOSTON MICROMACHINES CORPORATION
SHAPING LIGHT

Voltage/Deflection Data

Voltage versus Deflection Data

Voltage (V)	4x4 Region Deflection (nm)	Single Actuator Deflection (nm)
0	0	1
25	116	31
50	440	125
75	933	289
100	1502	519
125	2081	822
150	2653	1187
175	3232	1609
200	3843	2069
225	4532	2569
250	5431	3115
255	5681	3233

C.2 Camera Datasheet

Pixelink PL-D775MU-BL used for both the SHWFS and the science imager.

TECHNICAL SPECIFICATIONS

SENSOR	
Sensor	On Semi MT9P006 (color); On Semi MT9P031 (monochrome)
Type	CMOS Rolling Shutter
Resolution	5.0 MP (2592 x 1944)
Pixel Pitch	2.2 µm x 2.2 µm
Active Area	7.13 mm diagonal
Max Datarate	96 MHz
PERFORMANCE SPECIFICATIONS	
FPN	<1 % of signal
PRNU	<2.5 % of signal
Dynamic Range	60 dB
Bit Depth	8 or 12-bit
Responsivity	1.76V/lux-sec (550nm)
Color Data Formats	Bayer 8, Bayer 16 and YUV422
MECHANICALS	
Dimensions (mm)	32 x 48 x 11 (without lens mount)
Weight (g)	35.8 (without optics)
Mounting	C-Mount, S-Mount and CS-Mount
INTERFACES	
Interface | Date rate	USB 3.0 | Micro-B | 5Gbps
Board Level Trigger Connector	8-pin Molex 1.25mm pitch
Enclosed Trigger Connector	Hirose round 8-pin
Trigger Mode 0	Software and hardware
Board Level Trigger Input	1 input, 3.3V (with internal pullup resistor)
Enclosed Trigger Input	1 optically Isolated, 5-12V DC at 4-11 mA
Board Level GPO/Strobe	2 outputs, 3.3V
Enclosed GPO/Strobe	2 outputs, 3.3V and 1 optically isolated max 40V DC, max 15mA

FRAME RATE	
Resolution	Free Running
2592 x 1944	15 fps
1980 x 1020	32.4 fps
1280 x 1024	42.6 fps
640 x 480	127.4 fps

Frame rates will vary based on host system and configuration

*Above calculations based on fixed frame rate mode

POWER REQUIREMENTS	
Voltage Required	5V DC (from USB connector)

PIO INTERFACE PIN OUTPUT DESCRIPTION	
Pin	**Pin Name & Function**
1	3.3V power output
2	TRIGGER, 3.3V HCMOS input
3	Ground
4	GPO1, 3.3V HCMOS output
5	GPO2, 3.3V HCMOS output
6	Clock, 3.3V (12C access for OEMs)
7	Data, 3.3V (12C access for OEMs)
8	No connection

Board connector: Molex 53398-0871 (8-pin, 1.25mm pitch, vertical); Cable receptacle 51021-0800; Cable crimp terminals: Molex 50079-8100

ENCLOSED GPIO INTERFACE PIN OUTPUT DESCRIPTION	
1	VBUS (Power output from USB3 cable)
2	TRIGGER + (optically isolated)
3	TRIGGER - (optically isolated)
4	GPO1 + (optically isolated)
5	GPO1 - (optically isolated)
6	GPO1, 3.3V HCMOS output
7	GPO2, 3.3V HCMOS output
8	Ground (logic and chassis ground)

SOFTWARE	
PixeLINK Capture	Test and Configuration Software
DirectShow	Bundled with PixeLINK Capture
TWAIN	Bundled with PixeLINK Capture
SDK	API, sample code and LABVIEW wra

ENVIRONMENTAL & REGULATORY	
Compliance	FCC Class B, CE & RoHS
Shock & Vibration	300 G & 20 G (10Hz - 2KHz)
Operating Temperature	0°C to 50°C (non-condensing)
Storage Temperature	-45°C to 85°C

COMPUTER & OPERATING SYSTEM				
	Windows	**Linux x86**	**Linux ArmV7**	**Linu Arm**
Processor	Intel i5 or better	Intel i5 or better	Arm7 (32 bit)	Arm bit)
Memory	4GB recom-mended	4GB recom-mended	2GB	2GB
Hard Drive Space	150 MB	150 MB	50 MB	50 M
Operating System	Windows 7/8/10	Ubuntu 14.04 / 16.04 Desktop	Ubuntu 14.04 Desktop	Ubu 14.0 Des

Appendix D

Zonal Reconstruction Implementation

The implmentation of zonal reconstruction used in this thesis is based on a MATLAB example in [50].

The main function is:

```
import numpy as np
import astropy.units as u
def zonalReconstruction(x,y,ds):
    #flatten operates in row-major order
    g=np.concatenate(np.nan_to_num([x.flatten().to(u.radian),
        y.flatten().to(u.radian)]))
    m=x.shape[0]
    n=x.shape[1]
    S=g

    print("m:",m,"n:",n)
    E = getE(m,n)
    C = getC(m,n)

    C=np.matrix(C)
    S=np.matrix(S)
```

```
    Epinv = np.linalg.pinv(E)
    p=Epinv*C*S.T
    return np.multiply(p.reshape(m,n),ds)
```

The example has been adapted to build the matrices E and C for a rectangular lenslet array:

```
def getC(m,n):
    C = np.matrix(np.zeros([(m-1)*n+(n-1)*m, 2*n*m]))

    for i in range(m):
        for j in range(n-1) :
                C[i*(n-1)+j, i*n+j]=0.5
                C[i*(n-1)+j, i*n+j+1]=0.5
    for i in range(n):
        for j in range(m-1):
                C[m*(n-1)+i*(m-1)+j, n*(m+j)+i]=0.5
                C[m*(n-1)+i*(m-1)+j, n*(m+j+1)+i]=0.5
    return C


def getE(m,n):
    E=np.matrix(np.zeros([(m-1)*n+(n-1)*m, n*m]))
    for i in range(m):
        for j in range(n-1):
            E[i*(n-1)+j, i*n+j] = -1
            E[i*(n-1)+j, i*n+j+1] = 1
    for i in range(n):
        for j in range(m-1):
            E[m*(n-1)+i*(m-1)+j, i+j*n] = -1
            E[m*(n-1)+i*(m-1)+j, i+(j+1)*n] = 1
    return E
```

Bibliography

[1] Gary Chanan. Principles of Wavefront Sensing and Reconstruction. *Center for Adaptive Optics (CfAO) Proceedings: Summer School on Adaptive Optics*, pages 5–40, 2000.

[2] John W. Hardy. *Adaptive Optics for Astronomical Telescopes*. Oxford University Press, US, 1998.

[3] Johanan L. Codona. Differential optical transfer function wavefront sensing. *Optical Engineering*, 52(9):097105, 2013.

[4] Lick Observatory. Introduction to adaptive optics and its history. `http://www.ucolick.org/~max/History_AO_Max.htm`.

[5] Jason B. Stewart, Daniel V. Murphy, John D. Moores, Andrew S. Fletcher, and Keith M. Bonneau. Comparing adaptive optics approaches for NASA LCRD Ground Station #2. *Proc. SPIE*, 8610(March 2013):86100M, 2013.

[6] Stanislav Gordeyev, Tim E. Hayden, and Eric J. Jumper. Aero-Optical and Flow Measurements Over a Flat-Windowed Turret. *AIAA Journal*, 45(2):347–357, 2007.

[7] Martin J. Booth. Adaptive optics in microscopy. *Philosophical Transactions of the Royal Society A: Mathematical, Physical and Engineering Sciences*, 365(1861):2829–2843, 2007.

[8] Catalog, the extrasolar planets encyclopaedia. `http://exoplanet.eu/catalog/`. Accessed: 2018-08-18.

[9] Christophe Lovis and Debra A Fischer. Radial Velocity Techniques for Exoplanets. In *Exoplanets*, pages 27–53. 2010.

[10] J. N. Winn. Exoplanet Transits and Occultations. In *Exoplanets*, pages 55–77. 2010.

[11] W. A. Traub and B. R. Oppenheimer. Direct Imaging of Exoplanets. In *Exoplanets*, pages 111–156. 2010.

[12] D Mawet, E Serabyn, K Liewer, Ch Hanot, S McEldowney, D Shemo, and N O'Brien. Optical Vectorial Vortex Coronagraphs using Liquid Crystal Polymers: theory, manufacturing and laboratory demonstration. *Optics express*, 17(3):1902–1918, 2009.

[13] Aki Roberge, Maxime J. Rizzo, Andrew P. Lincowski, Giada N. Arney, Christopher C. Stark, Tyler D. Robinson, Gregory F. Snyder, Laurent Pueyo, Neil T. Zimmerman, Tiffany Jansen, Erika R. Nesvold, Victoria S. Meadows, and Margaret C. Turnbull. Finding the needles in the haystacks: High-fidelity models of the modern and Archean solar system for simulating exoplanet observations. *Publications of the Astronomical Society of the Pacific*, 129(982):1–22, 2017.

[14] Olivier Guyon. Limits of Adaptive Optics for high contrast imaging. *The Astrophysical Journal*, 629(1):592–614, 2005.

[15] Jared R. Males and Olivier Guyon. Ground-based adaptive optics coronagraphic performance under closed-loop predictive control. *Journal of Astronomical Telescopes, Instruments, and Systems*, 4(1), 2017.

[16] Craig Underwood, Sergio Pellegrino, Vaios Lappas, Chris Bridges, Ben Taylor, Savan Chhaniyara, Theodoros Theodorou, Peter Shaw, Manan Arya, James Breckinridge, Kristina Hogstrom, Keith D Patterson, John Steeves, and Lee Wilson. SSC-VI-5 Autonomous Assembly of a Reconfiguarble Space Telescope (AAReST) âĂŞ A CubeSat / Microsatellite Based Technology Demonstrator. *27th Annual AIAA/USU Conference on Small Satellites*, 2013.

[17] James A Champagne, Scott M Hansen, Trent T Newswander, and Blake G Crowther. SSC14-VII-2 CubeSat Image Resolution Capabilities with Deployable Optics and Current Imaging Technology Conference on Small Satellites. *Proceedings of the AIAA/USU Conference on Small Satellites*, 2014.

[18] Thomas G. Bifano. Microelectromechanical deformable mirrors. *IEEE Journal on Selected Topics in Quantum Electronics*, 5(1):83–89, 1999.

[19] Benjamin Potsaid and John Ting-Yung Wen. Adaptive scanning optical microscope: large field of view and high-resolution imaging using a MEMS deformable mirror. *Journal of Micro/Nanolithography, MEMS, and MOEMS*, 7(2):021009, 2008.

[20] Laurent Pueyo, Neil Zimmerman, Matthew Bolcar, Tyler Groff, Christopher Stark, Garreth Ruane, Jeffrey Jewell, Ji Wang, David Redding, Johan Mazoyer, Kevin Fograty, Roser Juanola-Parramon, shawn Domagal-Goldman, Aki Roberge, Avi Mandell, Olivier Guyon, Remi Soummer, and Katheryn St Laurent. The LUVOIR architecture "A" coronagraph instrument. *UV/Optical/IR Space Telescopes and Instruments: Innovative Technologies and Concepts VIII*, (September 2017):15, 2017.

[21] S. Nam, S. Artikova, T. Chung, G. Garipov, J. A. Jeon, S. Jeong, J. Y. Jin, B. A. Khrenov, J. E. Kim, M. Kim, Y. K. Kim, P. Klimov, J. Lee, H. Y. Lee, G. W. Na, S. J. Oh, M. Panasyuk, I. H. Park, J. H. Park, Y. S. Park, B. W. Yoo, and H. J. Yoo. A telescope for observation from space of extreme lightnings in the upper atmosphere. *Nuclear Instruments and Methods in Physics Research, Section A: Accelerators, Spectrometers, Detectors and Associated Equipment*, 588(1-2):197–200, 2008.

[22] Jin-A Jeon, Hye Young Lee, Ji Eun Kim, Jik Lee, and Il H. Park. Performance of the second MEMS space telescope for observation of extreme lightning from space. *Journal of the Korean Physical Society*, 68(5):710–714, 2016.

[23] Brian T Fleming, Stephan R Mccandliss, Keith Redwine, Mary Elizabeth, Paul D Feldman, Alexander S Kutyrev, Mary J Li, S H Moseley, John Vallerga, and Adrian Martin. Calibration and Flight Qualification of FORTIS. In *Proceedings of SPIE*, volume 8859, page 88590Q, 2013.

[24] Ewan S Douglas, Christopher B Mendillo, Timothy A Cook, Kerri L Cahoy, and Supriya Chakrabarti. Wavefront sensing in space : flight demonstration II of the PICTURE sounding rocket payload Wavefront sensing in space : flight demonstration II of the PICTURE sounding rocket payload. *Astron. Telesc. Instrum. Syst.*, 4(1):019003, 2018.

[25] Kerri L. Cahoy, Anne D. Marinan, Benjamin Novak, Caitlin Kerr, Tam Nguyen, Matthew Webber, Grant Falkenburg, and Andrew Barg. Wavefront control in space with MEMS deformable mirrors for exoplanet direct imaging. *Journal of Micro/Nanolithography, MEMS, and MOEMS*, 13(1):011105, 2013.

[26] E.S. Douglas, G. Allan, D. Barnes, J.S. Figura, C.A. Haughwout, J.N. Gubner, A.A. Knoedler, S. Leclair, T.J. Murphy, N. Skouloudis, J. Merck, R.A. Opperman, and K.L. Cahoy. Design of the deformable mirror demonstration CubeSat (DeMi). *Proceedings of SPIE - The International Society for Optical Engineering*, 10400(Dm), 2017.

[27] Anne Marinan, Kerri Cahoy, John Merk, Ruslan Belikov, and Eduardo Bendek. Improving Nanosatellite Imaging with Adaptive Optics. *AIAA/USU Conference on Small Satellites*, August 2016. `http://digitalcommons.usu.edu/smallsat/2016/S8InstSciMis/4`.

[28] John Merk, Kerri Cahoy, and Ewan Douglas. Deformable mirror (demi) cubesat system requirements review. Technical report, Aurora Flight Sciences, Cambridge, Massachusetts.

[29] Amir Give'on, Brian Kern, Stuart Shaklan, Dwight C. Moody, and Laurent Pueyo. Broadband wavefront correction algorithm for high-contrast imaging systems. In *Proc. SPIE*, volume 6691, page 66910A, 2007.

[30] Shanti R. Rao, J. Kent Wallace, Rocco Samuele, Supriya Chakrabarti, Timothy Cook, Brian Hicks, Paul Jung, Benjamin Lane, B. Martin Levine, Chris Mendillo, Edouard Schmidtlin, Mike Shao, and Jason B. Stewart. Path length control in a nulling coronagraph with a MEMS deformable mirror and a calibration interferometer. In *Proc. SPIE*, volume 6888, pages 68880B–68880B–9, 2008.

[31] Eduardo Bendek, Dana Lynch, Eugene Pluzhnik, Ruslan Belikov, Benjamin Klamm, Elizabeth Hyde, and Katherine Mumm. Development of a miniaturized deformable mirror controller. In *Proc. SPIE*, volume 9909, page 990984, 2016.

[32] Cal Poly SLO. 6U CubeSat Design Specification Rev. PROVISIONAL. `http://www.cubesat.org/s/6U_CDS_2016-05-19_Provisional.pdf`, April 16.

[33] James Paul Mason, Matt Baumgart, Bryan Rogler, Chloe Downs, Margaret Williams, Thomas N. Woods, Scott Palo, Phillip C. Chamberlin, Stanley Solomon, Andrew Jones, Xinlin Li, Rick Kohnert, and Amir Caspi. MinXSS-1 CubeSat On-Orbit Pointing and Power Performance: The First Flight of the Blue Canyon Technologies XACT 3-axis Attitude Determination and Control System. *Journal of Small Satellites*, 6(3):651–662, 2017.

[34] Christopher M. Pong, Matthew W. Smith, Matthew W. Knutson, Sungyung Lim, David W. Miller, Sara Seager, Jesus S. Villaseñor, and Shawn D. Murphy. One-arcsecond line-of-sight pointing control on exoplanetsat, a three-unit CubeSat. *Advances in the Astronautical Sciences*, 141:147–166, 2011.

[35] M. Konnik and J. De Dona. Waffle mode mitigation in adaptive optics systems: a constrained Receding Horizon Control approach. *2013 American Control Conference (Acc)*, (June 2013):3390–3396, 2013.

[36] François Roddier. Curvature sensing and compensation: a new concept in adaptive optics. *Applied Optics*, 27(7):1223, 1988.

[37] Roberto Ragazzoni. Pupil plane wavefront sensing with an oscillating prism. *Journal of Modern Optics*, 43(2):289–293, 1996.

[38] S. Esposito and A. Riccardi. Pyramid Wavefront Sensor behavior in partial correction Adaptive Optic systems, 2001.

[39] Olivier Guyon. Ao system design: Astronomy, Aug 2018.

[40] J. R. Fienup. Phase retrieval algorithms: a comparison. *Applied Optics*, 21(15):2758, 1982.

[41] R W Gerchberg and W O Saxton. A Practical Algorithm for the Determination of Phase from Image and Diffraction Plane Pictures. *Optik*, 35(2):237, 1972.

[42] Robert A. Gonsalves. Phase Retrieval And Diversity In Adaptive Optics. *Optical Engineering*, 21(5), 1982.

[43] Johanan L. Codona and Nathan Doble. James Webb Space Telescope segment phasing using differential optical transfer functions. *Journal of Astronomical Telescopes, Instruments, and Systems*, 1(2):029001, 2015.

[44] W.H. Southwell. Wave-front estimation from wave-front slope measurements. *Journal of the Optical Society of America*, 70(8):998, 1980.

[45] J. A. Butterworth. Wavefront Aberration Correction Using Zernike Polynomial Parameterizations of Optical Phased Arrays. *American Control Conference*, (July 2007), 2007.

[46] Alice M. Nightingale and Stanislav Gordeyev. Shack-Hartmann wavefront sensor image analysis: a comparison of centroiding methods and image-processing techniques. *Optical Engineering*, 52(7):071413, 2013.

[47] sckikit-image : image processing in python. `https://scikit-image.org/`.

[48] Seung-Whan Bahk. Highly accurate wavefront reconstruction algorithms over broad spatial-frequency bandwidth. *Optics Express*, 19(20):18997, 2011.

[49] Lisa A. Poyneer, Donald T. Gavel, and James M. Brase. Fast wave-front reconstruction in large adaptive optics systems with use of the Fourier transform. *J. Opt. Soc. Am. A*, 19(10):2100–2111, 2002.

[50] Guang-ming Dai. Chapter 4 Ocular Wavefront Sensing and Reconstruction. *Wavefront Optics for Vision Correction*, 1, 2008.

[51] Jan Herrmann. Least-squares wave front errors of minimum norm. *Journal of the Optical Society of America*, 70(1):28–35, 1980.

[52] Marshall Perrin. Physical optics propagation in python (poppy). `https://poppy-optics.readthedocs.io/`.

[53] J.W. Goodman. *Introduction to Fourier Optics*. 3 edition, 2005.

[54] Miguel Arevallilo Herráez, David R. Burton, Michael J. Lalor, and Munther A. Gdeisat. Fast two-dimensional phase-unwrapping algorithm based on sorting by reliability following a noncontinuous path. *Applied Optics*, 41(35):7437, 2002.

[55] Jinsheng Yang, Ling Wei, Hongli Chen, Xuejun Rao, and Changhui Rao. Absolute calibration of Hartmann-Shack wavefront sensor by spherical wavefronts. *Optics Communications*, 283(6):910–916, 2010.

[56] Alexander Chernyshov, Uwe Sterr, Fritz Riehle, Jürgen Helmcke, and Johannes Pfund. Calibration of a Shack-Hartmann sensor for absolute measurements of wavefronts. *Applied Optics*, 44(30):6419, 2005.

[57] Alexander T. Rodack, Justin M. Knight, Johanan L. Codona, Kelsey L. Miller, and Olivier Guyon. Adaptive optics self-calibration using differential OTF (dOTF). In *Proc. SPIE*, number 9605, 2015.

[58] Justin M. Knight, Alexander T. Rodack, Johanan L. Codona, Kelsey L. Miller, and Olivier Guyon. Deconvolution of differential OTF (dOTF) to measure high-resolution wavefront structure. In *Proc. SPIE*, volume 9605, 2015.

[59] E. Candes, X. Li, and M. Soltanolkotabi. Phase Retrieval via Wirtinger Flow: Theory and Algorithms. *ArXiv e-prints*. `https://arxiv.org/abs/1407.1065`.